

1 Local wind regime induced by giant linear dunes:  
2 comparison of ERA5-Land ~~re-analysis~~ reanalysis  
3 with surface measurements

4 Cyril Gadal · Pauline Delorme ·  
5 Clément Narteau · Giles F.S. Wiggs ·  
6 Matthew Baddock · Joanna M. Nield ·  
7 Philippe Claudin

8  
9 Received: DD Month YEAR / Accepted: DD Month YEAR

10 **Abstract**

11 Emergence and growth of sand dunes results from the dynamic interaction be-  
12 tween topography, wind flow and sediment transport. While feedbacks between  
13 these variables are well studied at the scale of a single and relatively small dune,  
14 the average effect of a periodic large-scale dune pattern on atmospheric flows  
15 remains poorly constrained, due to a pressing lack of data in major sand seas.  
16 Here, we compare field local measurements of surface wind data winds to the  
17 predictions of the ERA5-Land climate reanalysis at four locations in Namibia,  
18 including within the giant-dune both within and outside the giant linear dune  
19 field of the Namib sand seaSand Sea. In the desert plains to the north of  
20 the sand sea, observations and predictions agree well. This is also the case in  
21 the interdune areas of the sand sea, except for the weak winds blowing at  
22 night, which exhibit additional components during the day. During the night,

C. Gadal

Institut de Mécanique des Fluides de Toulouse, Université de Toulouse Paul Sabatier, CNRS,  
Toulouse INP-ENSEEIHT, Toulouse, France. E-mail: cyril.gadal@imft.fr

P. Delorme

Energy and Environment Institute, University of Hull, Hull, UK.

C. Narteau

Institut de Physique du Globe de Paris, Université de Paris, CNRS, Paris, France.

G. Wiggs

School of Geography and the Environment, University of Oxford, Oxford, UK.

M.C. Baddock

Geography and Environment, Loughborough University, Loughborough, UK.

J.M. Nield

School of Geography and Environmental Science, University of Southampton, Southampton,  
UK.

P. Claudin

Physique et Mécanique des Milieux Hétérogènes, CNRS, ESPCI Paris, PSL Research Uni-  
versity, Université de Paris, Sorbonne Université, Paris, France.

however, an additional wind component aligned with the giant dune orientation, which are not measured, in contrast to the easterly wind predicted by the ERA5-Land reanalysis. We quantify these similarities and differences and provide a physical understanding of the relevant aerodynamical regimes to relate them. For the given dune orientation and measured wind regime, we link the observed wind deviation (over 50°) to the daily cycle of the turbulent atmospheric boundary layer over a dune pattern of given wavelength. We conclude by identifying the conditions under which the ERA5-Land reanalysis data can reliably be used to study dune morphodynamics. We also propose that, in multidirectional wind regimes, deflections of specific winds. During the night, a shallow boundary layer induces a flow confinement above the giant dunes, resulting in large flow deviations, especially for the slower easterly winds. During the day, the feedback of the giant dunes on the atmospheric flow is much weaker due to the thicker boundary layer and higher wind speeds. Finally, we propose that the confinement mechanism and the associated wind deflections induced by giant dunes could explain the occurrence of secondary dune patterns with a different orientation to the primary structures between which they develop. development of smaller-scale secondary dunes, which elongate obliquely in the interdune areas of the primary dune pattern.

**Keywords** Atmospheric boundary layer · Sand dunes · Flow over hills

## 43 1 Introduction

44 The description of turbulent flows over complex topography is relevant for a  
45 large variety of different environmental systems (Finnigan et al. 2020)(Sherman 1978; Walmsley et al. 1982; Baines 1995;  
46 . For example, the flow over hills is of primary interest for wind power, me-  
47 teorological and air pollution phenomena (Taylor et al. 1987). The prop-  
48 erties of these flows are also key to the understanding of geophysical phe-  
49 nomena, including the formation of wind-driven waves on the ocean surface  
50 (Sullivan and McWilliams 2010), dissolution bedforms (Claudin et al. 2017)  
51 (Claudin et al. 2017; Guérin et al. 2020), or sedimentary ripples and dunes  
52 (Charru et al. 2013; Courrech du Pont 2015)(Bagnold 1941; Charru et al. 2013; Courrech du Pont 2015)  
53 . Importantly, the troposphere presents a vertical structure, with a lower con-  
54 vective boundary layer, of typical kilometer-scale thickness, capped by a stably  
55 stratified region (Stull 1988). The largest topographic obstacles, such as moun-  
56 tains, can therefore interact with this upper region and lead to internal wave  
57 generation or significant wind disturbances, such as lee-side downslope winds  
58 (Durran 1990).

59 ~~Focusing on the wind close to the surface, two related~~ Compared to hills and  
60 ~~mountains, aeolian sand dunes offer idealized elevation profiles for the study~~ of atmospheric turbulent flow over topographies, due to their smooth shape,  
61 ~~free of canopies. Besides, dunes provide a rather wide range of scales, from~~ decameters to kilometers, and very often come in a fairly regular pattern, which  
62 ~~further simplifies the flow structure analysis. Past studies have highlighted~~ two important topographic feedbacks on the ~~windflow over dunes can be~~  
63 ~~commented on separately~~ wind flow close to the dune/hill surface. First is the  
64 effect on wind speed, with documented flow acceleration on upwind slopes  
65 (Weaver and Wiggs 2011) and deceleration on downwind slopes (Baddock et al.  
66 2007), where the speed-up factor is essentially proportional to the obstacle  
67 aspect ratio (Jackson and Hunt 1975). ~~Importantly, the velocity maximum Under~~ Under  
68 ~~multidirectional wind regimes with frequent wind reversals, this speed-up effect~~ multidirectional wind regimes with frequent wind reversals, this speed-up effect  
69 ~~induces large differences in the amplitude and orientation of the resultant~~ induces large differences in the amplitude and orientation of the resultant  
70 sediment transport between flat sand beds and the dune crests (Zhang et al. 2014; Rozier et al. 2019; Gao et al. 2021)  
71 . In addition, the position of maximum velocity is typically shifted upwind  
72 of the obstacle crest (Jackson and Hunt 1975; Cladlin et al. 2013). This be-  
73 haviour has been theoretically predicted by means of asymptotic analysis of a  
74 neutrally stratified boundary-layer flow over an obstacle of vanishing aspect ra-  
75 ~~tio (Jackson and Hunt 1975; Mason and Sykes 1979; Sykes 1980; Hunt et al. 1988; Belcher and Hunt 1998)~~ (Jackson and Hunt 1975; Mason and Sykes 1979; Sykes 1980; Hunt et al. 1988; Belcher and Hunt 1998; Kroy et al. 2002  
76 . Experiments in flumes (Zilker et al. 1977; Zilker and Hanratty 1979; Freder-  
77 ick and Hanratty 1988; Poggi et al. 2007; Bristow et al. 2022), in wind tunnels  
78 (Gong and Ibbetson 1989; Finnigan et al. 1990; Gong et al. 1996) and in  
79 field conditions ~~at all scales~~ (Taylor and Teunissen 1987; Cladlin et al. 2013;  
80 Fernando et al. 2019; Lü et al. 2021), have also documented this effect. Inter-  
81 estingly, a similar behaviour exists for the pressure perturbation, but with a  
82 slight downwind shift for the pressure minimum (Cladlin et al. 2021).

The second effect, much less studied, is the flow deflection that occurs when the incident wind direction is not perpendicular to the ridge crest. While predicted to be small (less than 10°) in the linear regime valid for shallow topography (Gadal et al. 2019), significant flow steering has been reported in the field on the downwind side of steep enough obstacles, such as mountain ranges (Kim et al. 2000; Lewis et al. 2008; Fernando et al. 2019), well-developed sand dunes (Walker et al. 2009; Hesp et al. 2015; Walker et al. 2017; Smith et al. 2017; de Winter et al. 2017; Tsoar and Yaalon 1983; Sweet and Kocurek 1990; Walker and Nickling 2002; Smith et al. 2017) and in particular coastal foredunes (e.g. Hunter et al. 1983; Rasmussen 1989; Walker et al. 2006, 2009; Hesp et al. 2015; Vink et al. 2017), mountain ranges (Kim et al. 2000; Lewis et al. 2008; Fernando et al. 2019), and valley topographies (Wiggs et al. 2002; Garvey et al. 2005).

For practical reasons, wind measurement Wind measurements over sand dunes has been have been mainly performed over small bedforms, typically a few meters high (corresponding to several tens of meters long) (e.g. Lancaster et al. (1996); McKenna Neuman et al. (1997); Sauermann et al. (2003); Andreotti et al. (2002); Walker and Nickling (2002); Weaver and Wiggs (2011)). Giant dunes (e.g. Mulligan 1988; Hesp et al. 1989; Lancaster et al. 1996). For practical reasons, fewer studies have performed similar measurements on giant dunes (Hayholm and Kocurek 1988), with kilometer-scale wavelengths and heights of tens of meters, are more difficult to investigate although for several reasons they. However, such large dunes provide a choice configuration for the study of turbulent flows over a complex topography. First, one expects larger wind disturbances for larger obstacles. Secondly, their large size makes can make them interact with the vertical structure of the atmosphere (Andreotti et al. 2009). Third, they usually form large patterns in sand seas and thus behave as rather clean periodic perturbations, in contrast with isolated dunes. Finally, because the morphodynamics of aeolian bedforms are is strongly dependent on the local wind regime (Livingstone and Warren 2019), one can expect to see the consequences of windflow disturbance by large dunes on neighbouring small dunes (Brookfield 1977; Ewing et al. 2006). A similar effect is observed on the properties of impact ripple patterns due to the presence of dunes (Howard 1977; Hood et al. 2021)(Howard 1977; Hood et al. 2021).

. Atmospheric flows have been much studied at the desert-scale with climate reanalyses based on global atmospheric models (Blumberg and Greeley 1996; Livingstone et al. 2010; Ashkenazy et al. 2012; Blumberg and Greeley 1996; Livingstone et al. 2010; Ashkenazy et al. 2012; Jolivet et al. 2021; Hu et al. 2021; Gunn et al. 2021), such as ERA-40, ERA-Interim or ERA5 (Uppala et al. 2005; Dee et al. 2011; Hersbach et al. 2020). However, the spatial resolution of these reanalyses (tens of kilometers) of these reanalyses implies average quantities that do not resolve the smaller scales of interest, which range from individual dunes to small mountains (Livingstone et al. 2010). Recently, the release of ERA5-Land has partly resolved this limitation by providing up to 70 years of hourly wind predictions at a 9 km spatial resolution (Muñoz-Sabater et al. 2021). However, its validity remains to be studied, especially in remote desert areas where assimilation of measured data is very low.

In this work, we compare local wind speeds and directions measured by meteorological stations at four different locations inside and north of the

133 ~~giant-dune giant linear dune~~ field of the Namib sand sea to the regional predictions  
134 of the ERA5-Land climate reanalysis. Where the meteorological stations  
135 are surrounded by a relatively flat environment, we show that local measurements  
136 and regional predictions agree well. The agreement is also good in the  
137 interdune areas of the sand sea, except for some weak winds blowing at night,  
138 which exhibit an additional component aligned with the giant dune orientation.  
139 These winds are not predicted by the ERA5-Land reanalysis (section 2 2).  
140 Further, we are able to link the magnitude of these differences to the circadian  
141 cycle of the atmospheric boundary layer (section 3 3). Finally, we draw  
142 implications for the wind disturbances on smaller-scale dunes (section 4 4),  
143 suggesting a possible origin for crossing dunes ~~a distinctive secondary dune~~  
144 ~~form observed in the Namib and other sand seas.~~

## 145 2 Wind regimes across the Namib Sand Sea

146 We measured the wind regime at four different locations in Namibia, repre-  
147 sentative of various arid environments across the Namib desert (Fig. 1, **Online**  
148 **Resource** Fig. 42). The Etosha West station was located at the Adamax wa-  
149 terhole to the west of Etosha Pan in northern Namibia, in a sparsely vegetated  
150 area. The Huab station was near the coast on a hyper-arid flat gravel plain  
151 lying north ~~of~~ the ephemeral Huab river. Here, barchan dunes up to a few me-  
152 ters in height develop from the sediment blowing out of the river valley (Nield  
153 et al. 2017; Hesp and Hastings 1998). These two stations were both located  
154 in relatively flat environments. In contrast, the North Sand Sea and South  
155 Sand Sea stations were located in the interdunes between linear dunes with  
156 kilometer-scale wavelengths, hectometer-scale heights and superimposed pat-  
157 terns. In this section, we describe and compare winds from local measurements  
158 and climate reanalysis predictions.

### 159 2.1 Wind and elevation data

160 At each meteorological station (Fig. 1), wind speed and direction were sam-  
161 pled every 10 minutes using cup anemometers (Vector Instruments A100-LK)  
162 and wind vanes (Vector Instruments W200-P) at ~~heights which varied a single~~  
163 ~~height, which was~~ between 2 m and 3 m depending on the station. The avail-  
164 able period of measurements at each station ranged from 1 to 5 discontinuous  
165 years distributed between 2012 and 2020 (Online Resource Fig. S24). We  
166 checked that at least one complete seasonal cycle was available for each sta-  
167 tion. Regional winds were extracted at the same locations and periods from the  
168 ERA5-Land dataset, which is a replay at a smaller spatial resolution of ERA5,  
169 the latest climate reanalysis from the ~~ECMWWF~~-ECMWF (Hersbach et al.  
170 2020; Muñoz-Sabater et al. 2021). This dataset provided hourly predictions  
171 of the 10-m wind velocity and direction at a spatial resolution of  $0.1^\circ \times 0.1^\circ$   
172 ( $\simeq 9$  km in Namibia).

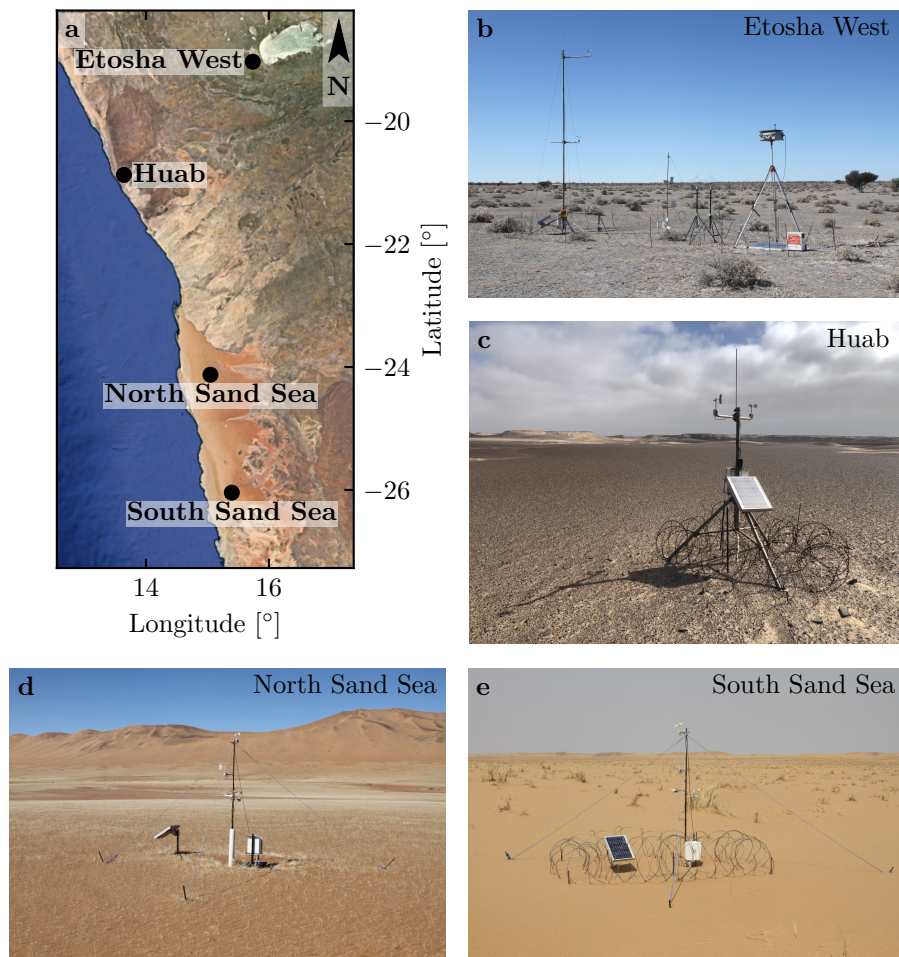


**Fig. 1** Wind data used in this study Studied field sites. **a:** Location of the different sites in Namibia. **b–e:** Satellite images Photographs of these different environments (Google-Earth, Maxar Technologies, CNES/Airbus). In each subplot, the left and right wind roses represent the data from the ERA5-Land climate reanalysis and the local wind stations, respectively. Note that the bars show the direction towards which the wind blows. The black dots show the location of local wind meteorological stations.

To enable direct comparison, the local wind measurements were averaged into 1-hr bins centered on the temporal scale of the ERA5-Land estimates (Online Resource Fig. S3S2). As the wind velocities of both datasets were provided at different heights, we converted them into shear velocities  $u_*$  (Online Resource section 1), characteristic of the turbulent wind profile. Wind roses in Fig. 1(b–e) show the resulting wind data.

Dune properties were computed using autocorrelation on the 30-m Digital Elevation Models (DEMs) of the shuttle radar topography mission (Farr et al.

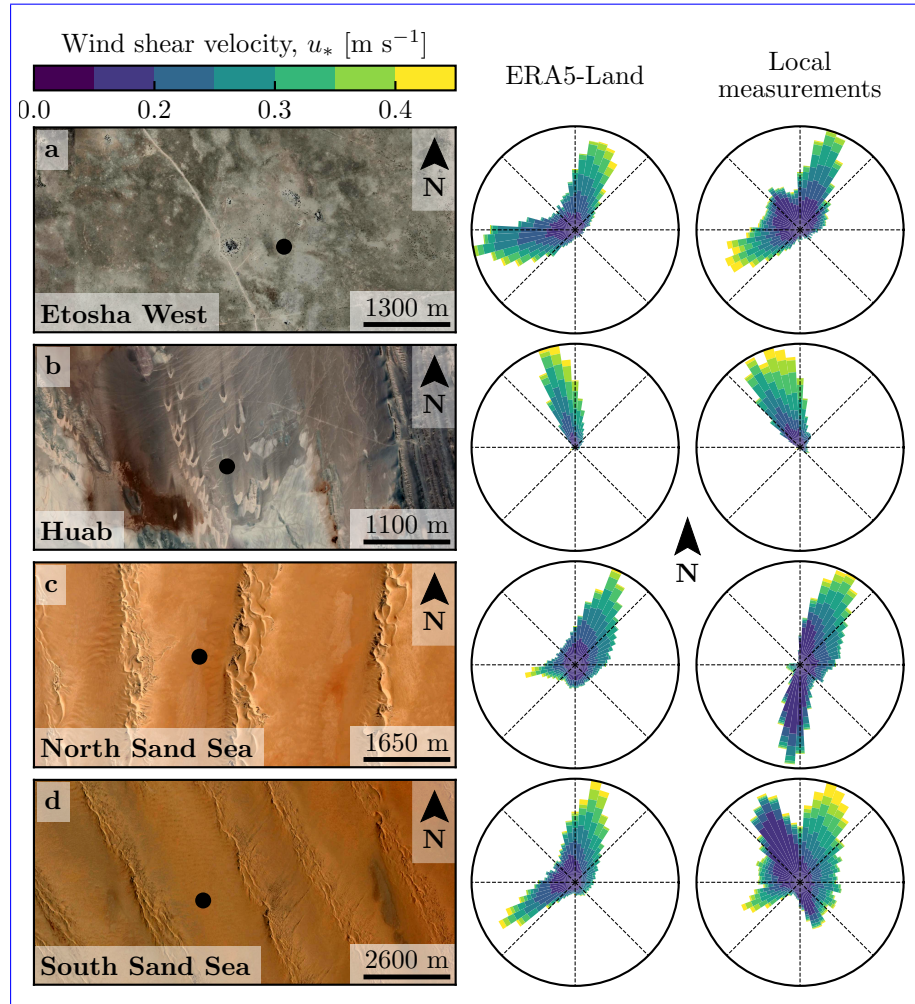


**Fig. 2** Wind data used in this study. Satellite images of the different environments (Google-Earth, Maxar Technologies, CNES/Airbus) are shown on the left. The black dots show the location of the wind measurements stations. On the right of the photos, the corresponding wind roses representing the data from the ERA5-Land climate reanalysis and the local wind stations are displayed. Note: the graphical convention for the wind roses is that the bars show the direction towards which the wind blows (see color bar for velocity scale).

181 2007). For the North and South Sand Sea stations, we obtain, respectively,  
 182 orientations of  $85^\circ$  and  $125^\circ$  with respect to the North, wavelengths of 2.6 km  
 183 and 2.3 km and amplitudes (or half-heights) of 45 m and 20 m (Online Resource  
 184 Fig. S5–S4 for more details). This agrees with direct measurements made on  
 185 site.

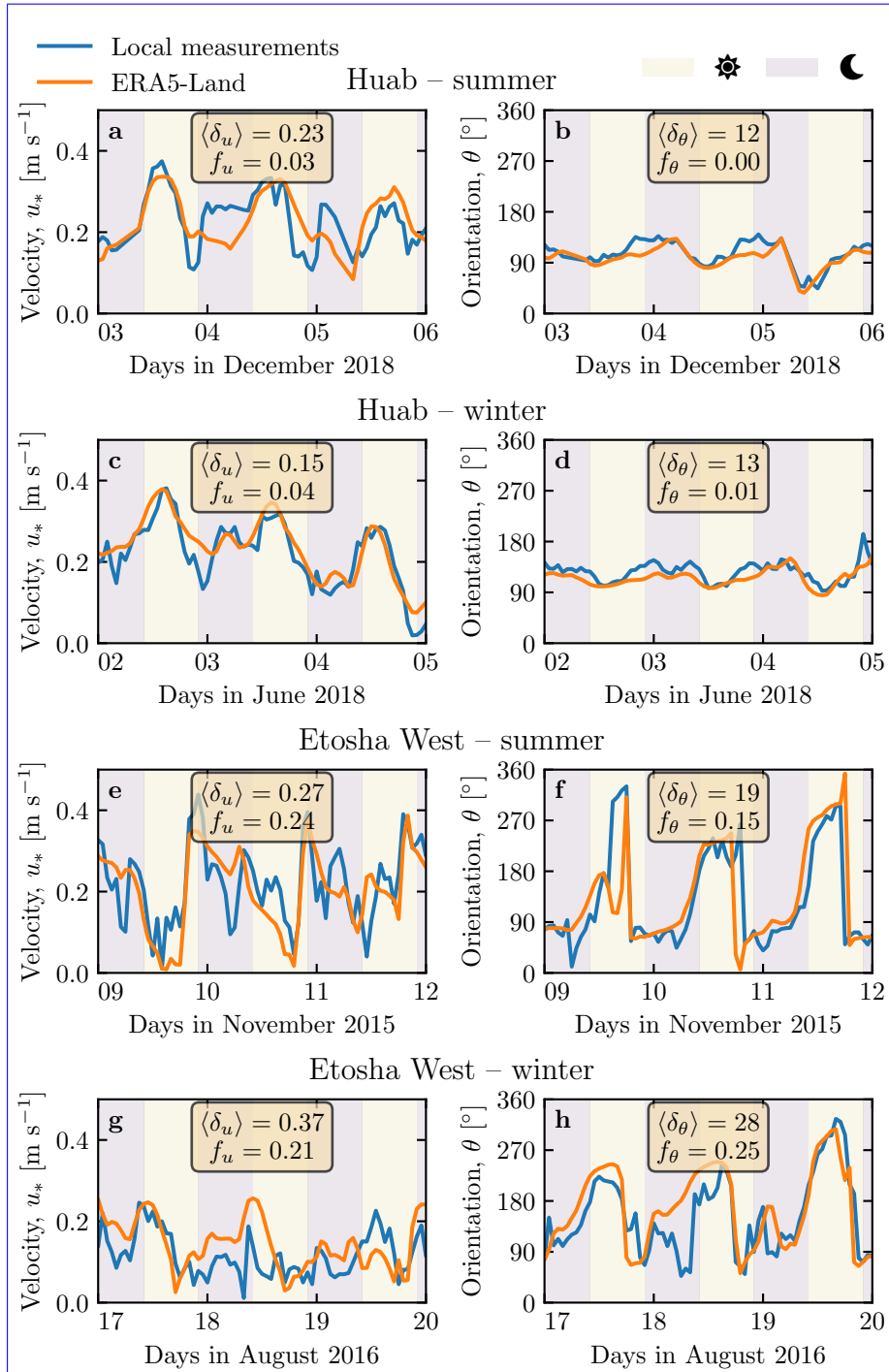


**Fig. 3** Temporal comparison between the wind data coming from the ERA5-Land climate reanalysis (orange lines) and from the local measurements (blue lines). Coloured swathes indicate day (between 1000–10.00 UTC and 2200–22.00 UTC) and night (before 1000–10.00 UTC or after 2200–22.00 UTC). Numbers in legends indicate the average flow deflection  $\delta_\theta$  and relative wind modulation  $\delta_u$  over the displayed period (see section 3.2 for their definitions), as well as the percentage  $f_\theta$  and  $f_u$  of occurrence of extreme events ( $\delta_\theta > 50^\circ$ ,  $|\delta_u| > 0.6$ ). **a–b:** Etosha West–Huab station in summer. **b–c:** Etosha West–Huab station in winter. **d–e:** North–Sand–Sea–Etosha West station in summer. **f–g:** North–Sand–Sea–Etosha West station in winter. Time series of the two other stations are shown in Online Resource Fig. S65.

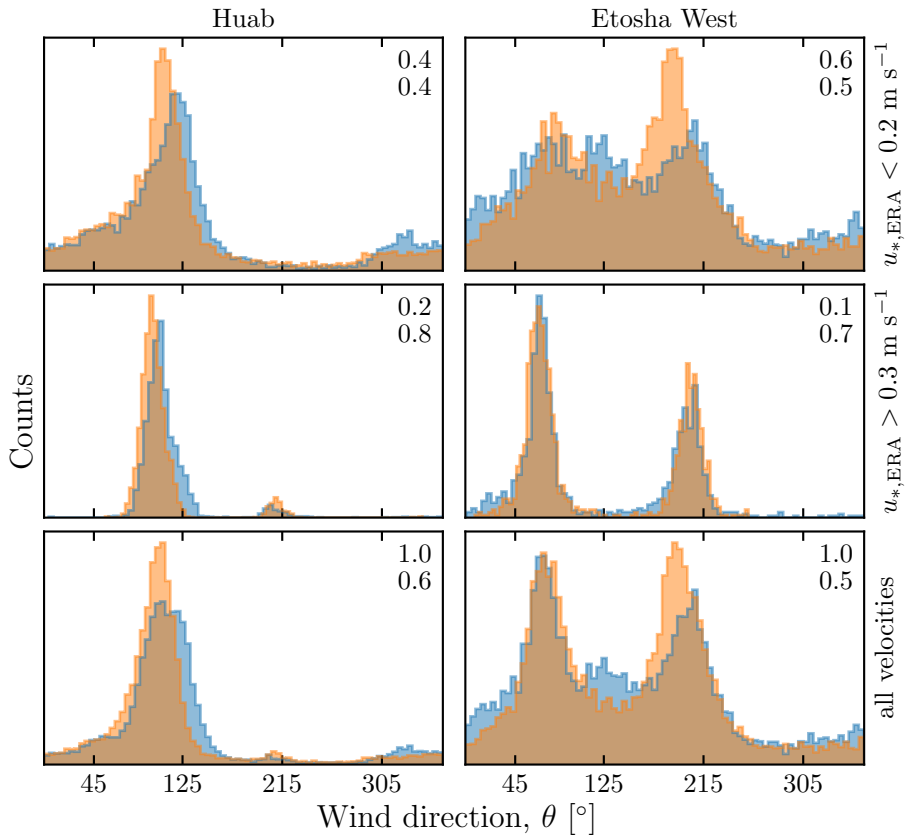


**Fig. 4** Distributions of wind direction at Huab and Etosha West stations for the ERA5-Land climate reanalysis (orange) and the local measurements (blue). In each subplot, both distributions are plotted from the same time steps, selected for different ranges of the wind wind velocity (rows) in the ERA5-Land dataset. The numbers at the upper right corners give the percentage of time steps selected in each sub-range (top), as well as the percentage of them corresponding to the day – defined between 10.00 UTC and 22.00 UTC (bottom).

## 186 2.2 Comparison of local and regional winds

187 The measured and predicted wind regimes are shown in Fig. 12. In the Namib,  
 188 the regional wind patterns are essentially controlled by the sea breeze, resulting  
 189 in strong northward components (sometimes slightly deviated by the large  
 190 scale topography) present in all regional wind roses (Lancaster 1985). These  
 191 daytime winds are dominant during the period October–March (Fig. 23f and  
 192 Online Resource Fig. S64f). During April–September, an additional (and often  
 193 nocturnal) easterly component can also be recorded, induced by the combina-  
 194 tion of katabatic winds forming in the mountains, and infrequent ‘berg’ winds,  
 195 which are responsible for the high wind velocities observed (Lancaster et al.  
 196 1984). The frequency of these easterly components decreases from inland to the  
 197 coast. As a result, bidirectional wind regimes within the Namib Sand Sea and

at the west Etosha site (Fig. 1b,d,e~~2a,c,d~~) and a unidirectional wind regime on the coast at the outlet of the Huab River (Fig. 4e~~2b~~) are observed.

In the case of the Etosha West and Huab stations, the time series of wind speed and direction from the regional predictions quantitatively match those corresponding to the local measurements (Fig. 2a-d) Figs. 3, 4 and Online Resource Figs. S6a-d, S7, S9 Fig. S5). For the North Sand Sea and South Sand Sea stations within the giant linear dune field, we observe that this agreement is also good, but limited to the October-March time period (Fig. 2e-h and and Online Resource Fig. S6e-h~~4a, b, e, f~~). However, the field-measured wind roses exhibit additional wind components aligned with the giant dune orientation, as evidenced on the satellite images (Fig. 42c,d).

More precisely, during the April-September period, the local and regional winds in the interdune match during daytime only, i.e. when the southerly/-southwesterly sea breeze dominates (Figs. 2e,f and 3, Online Resource Fig. S8~~5c,d,g,h and 6~~). In the late afternoon and during the night, when the easterly ‘berg’ and katabatic winds blow, measurements and predictions differ. In this case, the angular wind distribution of the local measurements exhibits two additional modes corresponding to reversing winds aligned with the giant dune orientation (purple frame in Fig. 36, Online Resource Figs. S8 and S10 Fig. S6). This deviation is also associated with a general attenuation of the wind strength (Online Resource Fig. S14S7). Remarkably, all these figures show that these wind reorientation and attenuation processes occur only at low velocities of the regional wind, typically for  $u_{*, ERA} \lesssim 0.2 \text{ m s}^{-1}$   $u_{*, ERA5-Land} \lesssim 0.2 \text{ m s}^{-1}$ . For shear velocities larger than  $u_{*, ERA} \approx 0.3 \text{ m s}^{-1}$   $u_{*, ERA5-Land} \approx 0.3 \text{ m s}^{-1}$ , the wind reorientation is not apparent. Finally, for intermediate shear velocities, both situations of wind flow reoriented along the dune crest and not reoriented can be successively observed (Online Resource Fig. S10S6). Importantly, these values are not precise thresholds (~~and certainly not related to the threshold for sediment transport~~), but indicative of a crossover between regimes, whose physical interpretation is discussed in the next section.

### 3 Influence of wind speed and circadian cycle on the atmospheric boundary layer

The wind deflection induced by linear dunes has previously been related to the incident angle between wind direction and crest orientation, with a maximum deflection evident for incident angles between 30° and 70° (Walker et al. 2009; Hesp et al. 2015). In the data analysed here, the most deflected wind at both the North and South Sand Sea stations is seen to be where the incident angle is perpendicular to the giant dunes (Figs. 4 and 3, Online Resource Fig. S8~~2 and 6~~). It therefore appears that in our case, the incident wind angle is not the dominant control on maximum wind deflection. Further, and as shown in Fig. 36, winds of high and low velocities show contrasting behaviour in characteristics of deflection. This suggests a change in hydrodynamical regime between the winds. In this section, we discuss the relevant parameters associ-

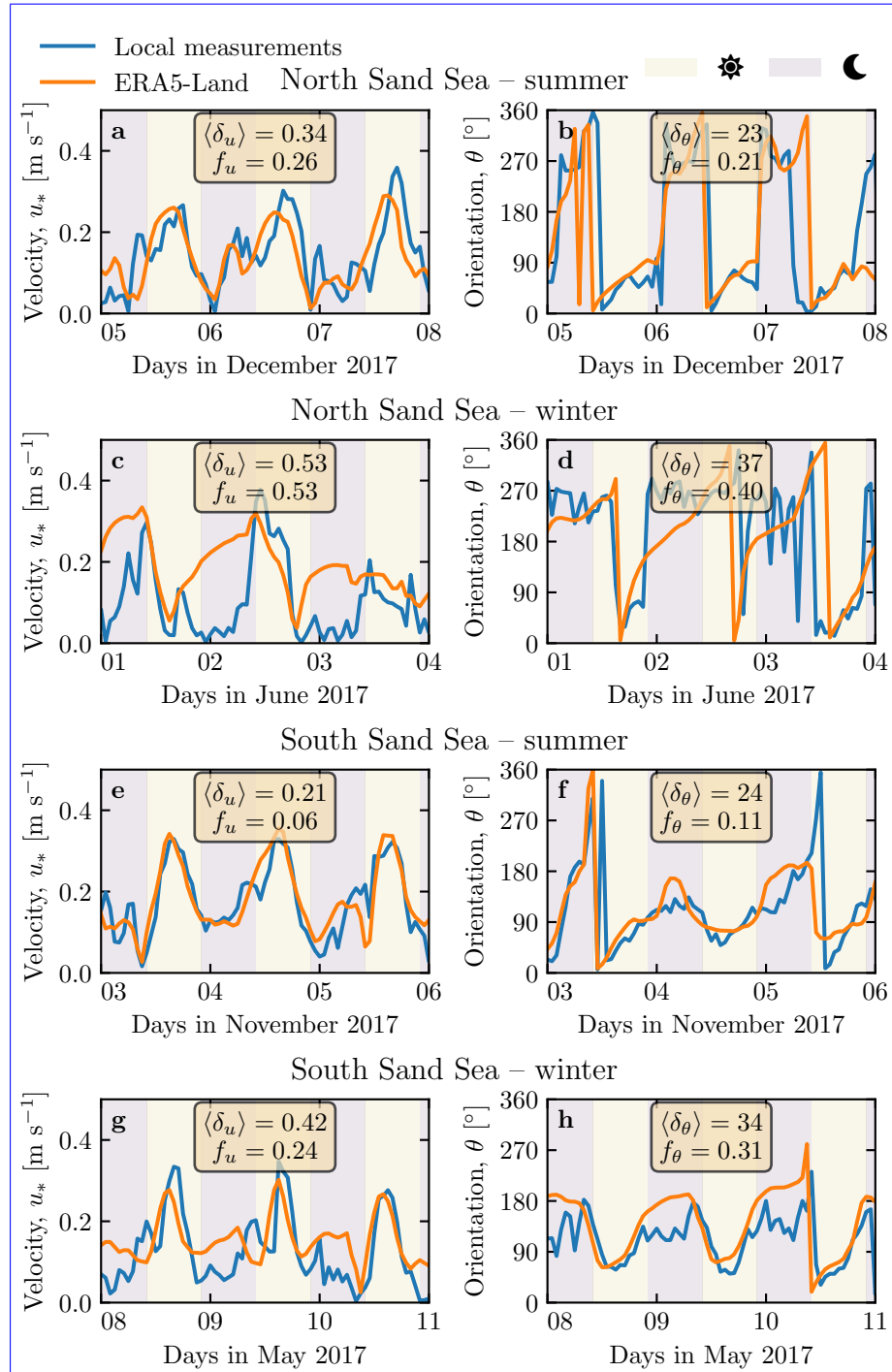


**Fig. 5** Distributions of wind direction at the Same as Fig. 3 for North Sand Sea Station for the ERA5 Land climate reanalysis (orange) and the local measurements station in summer (bluea–b). In each subplot, both distributions are plotted from the same time steps, selected with constraints on the wind direction (columns) and/or wind velocity (rows) of the ERA5 Land dataset. The grey vertical dashed lines indicate the dune orientation. The numbers at the top right give the percentage of time steps selected North Sand Sea station in each sub-range, as well as the percentage corresponding to the daytime winter (between 1000 UTC and 2200 UTCb–c). The purple frame highlights the regime (low wind velocities, nocturnal easterly wind) South Sand Sea station in which the data from both datasets differ. A similar figure can be obtained for the North summer (d–e) and South Sand Sea station in winter (Online Resource Fig. S8f–g).

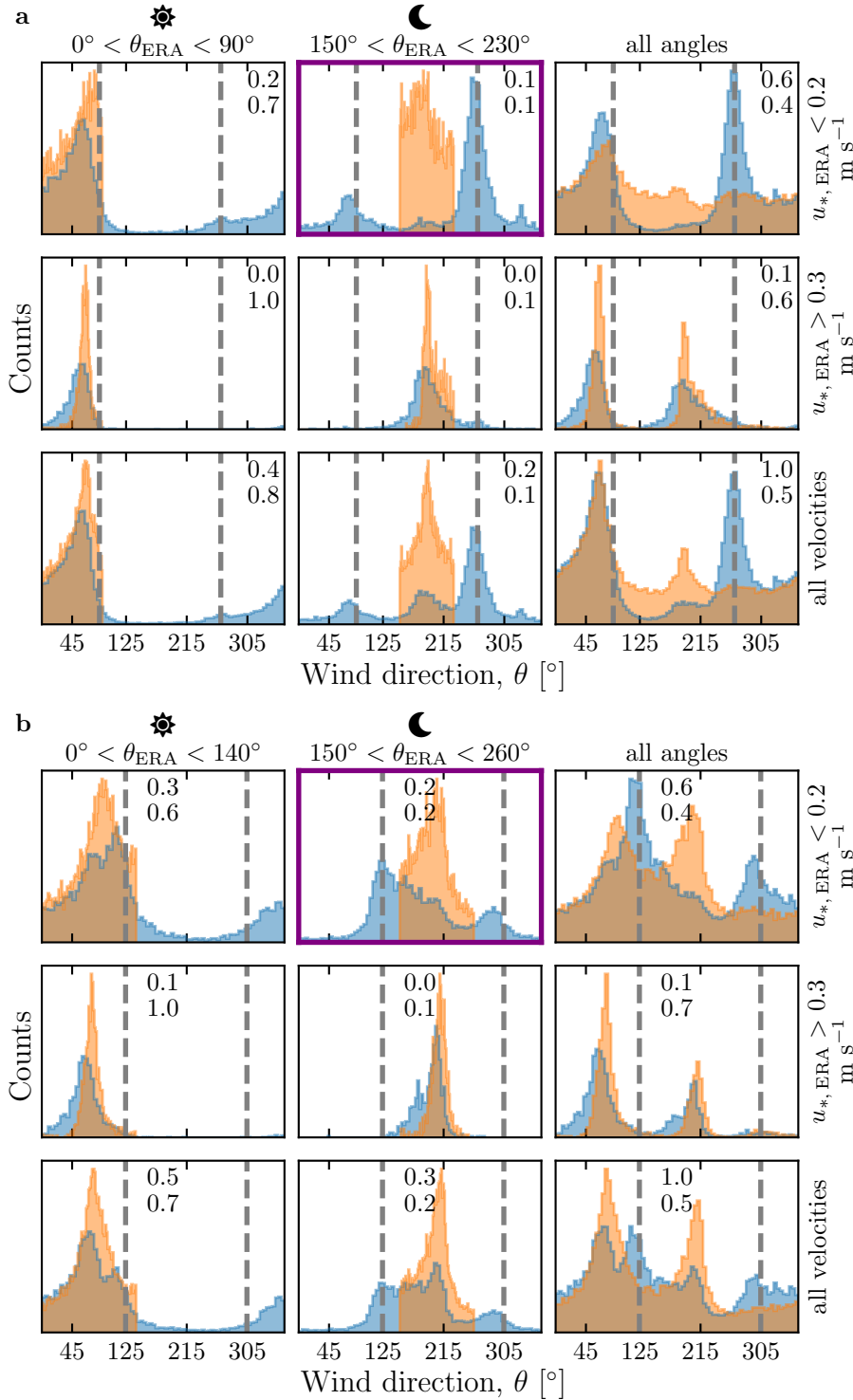


**Fig. 6** Same as Fig. 4 but for North Sand Sea (a) and South Sand Sea (b) stations. Here, subplots correspond to different ranges for the wind direction (columns) and wind velocity (rows) of the ERA5-Land dataset. The grey vertical dashed lines indicate the main dune orientation. In contrast with observations at the Huab and Etosha West stations (Fig. 4), histograms do not match well at low wind velocities, and the purple frame highlights the regime (low wind velocities, nocturnal easterly wind) in which the data from both datasets differ most.

241 ated with the dynamical mechanisms that govern the interactions between the  
242 atmospheric boundary layer flow and giant dune topographies. This analysis  
243 allows us to provide a physics-based interpretation of our measured wind data.

244 3.1 Flow over a modulated bed

245 Taking as a reference the turbulent flow over a flat bed, the general framework  
246 of our study is understanding and describing the flow response to a bed mod-  
247 ulation (e.g. a giant dune). Without loss of generality, we can consider in this  
248 context an idealised bed elevation in the form of parallel sinusoidal ridges, with  
249 wavelength  $\lambda$  (or wavenumber  $k = 2\pi/\lambda$ ) and amplitude  $\xi_0$ , and where the ref-  
250 erence flow direction makes a given incident angle with respect to the ridge  
251 crest (Andreotti et al. 2012). Part of this response, on which we focus here,  
252 is the flow deflection by the ridges. In a simplified way, it can be understood  
253 from the Bernoulli principle (Hesp et al. 2015): as the flow approaches the  
254 ridge crest, the compression of the streamlines results in larger flow velocities,  
255 and thus lower pressures ([Rubin and Hunter 1987](#)) ([Jackson and Hunt 1975](#)).  
256 An incident flow oblique to the ridge is then deflected towards lower pressure  
257 zones, i.e towards the crest. Turbulent dissipation tends to increase this effect  
258 downstream, resulting in wind deflection along the crest in the lee side (Gadal  
259 et al. 2019).

260 Flow confinement below a capping surface, which enhances streamline com-  
261 pression, has a strong effect on the hydrodynamic response and typically in-  
262 creases flow deflection. This is the case for bedforms forming in open channel  
263 flows such as rivers ([Fourrière et al. 2010; Unsworth et al. 2018](#)) ([Kennedy 1963](#); [Chang and Simons 1970](#); [Mizumura 1995](#)).  
264 . This is also relevant for aeolian dunes as they evolve in the turbulent atmo-  
265 spheric boundary layer (ABL) capped by the stratified free atmosphere (FA)  
266 (Andreotti et al. 2009). Two main mechanisms, associated with dimensionless  
267 numbers must then be considered (Fig. 47). First, topographic obstacles typi-  
268 cally disturb the flow over a characteristic height similar to their length. As  
269 flow confinement is characterised by a thickness  $H$ , the interaction between  
270 the dunes and the wind in the ABL is well captured by the parameter  $kH$ .  
271 The height  $H$  is directly related to the [radiative fluxes at sensitive heat flux](#)  
272 [from](#) the Earth surface. It is typically on the order of a kilometre, but sig-  
273 nificantly varies with the circadian and seasonal cycles. Emerging and small  
274 dunes, with wavelengths in the range 20 to 100 m, are not affected by the  
275 [flow](#) confinement, corresponding to  $kH \gg 1$ . For giant dunes with [kilometric](#)  
276 [kilometer-scale](#) wavelengths, however, their interaction with the FA [is-can be](#)  
277 significant (Andreotti et al. 2009). This translates into a parameter  $kH$  in the  
278 range 0.02–5, depending on the moment of the day and the season. A second  
279 important mechanism is associated with the existence of a thin intermediate  
280 so-called capping layer between the ABL and the FA. It is characterised by a  
281 density jump  $\Delta\rho$ , which controls the ‘rigidity’ of this interface, i.e. how much  
282 its deformation affects streamline compression. This is usually quantified using  
283 the Froude number (Vosper 2004; Stull 2006; Sheridan and Vosper 2006; Hunt

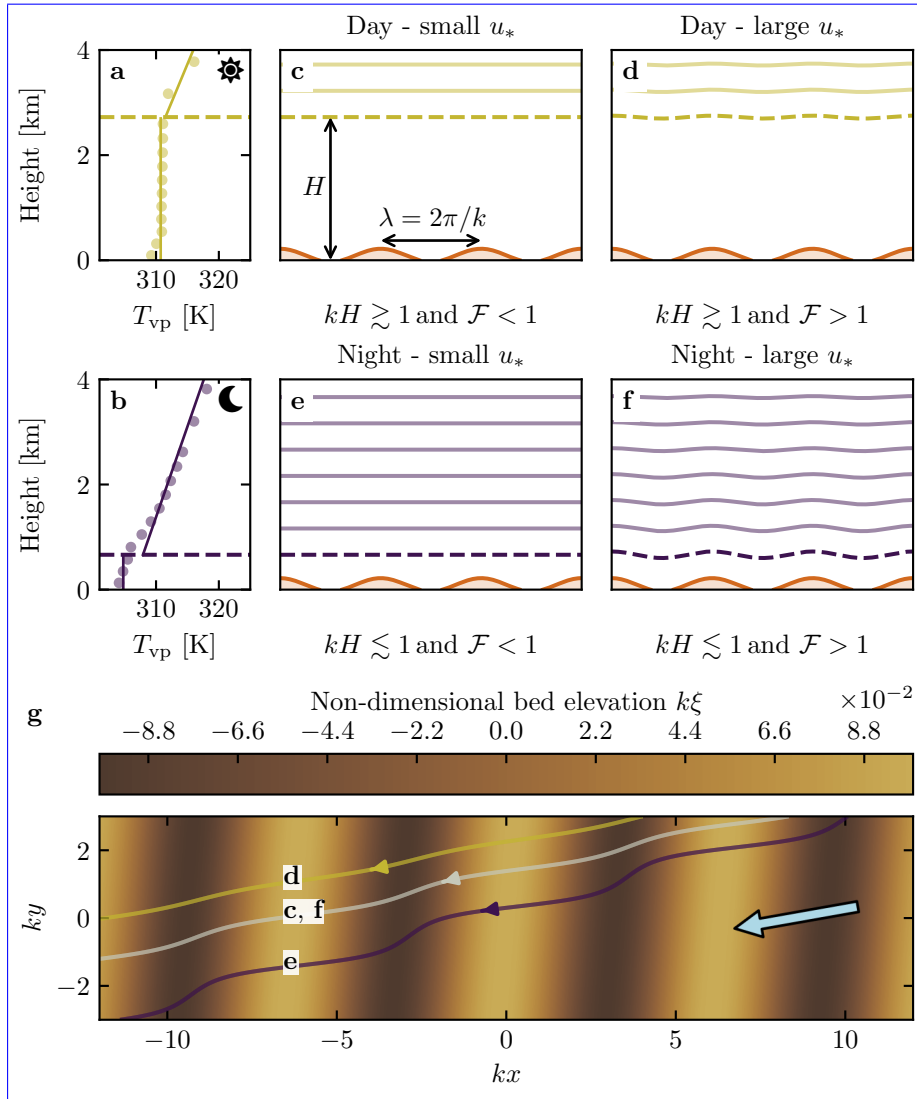


**Fig. 7** **a–b:** Vertical profiles of the virtual potential temperature  $T_{vp}$  at **two** different time steps (day - 03/11/2015 - **1200–12.00** UTC, night - 01/13/2013 - **0900–09.00** UTC) at the North Sand Sea station. Dots: data from the ERA5 reanalysis. Dashed lines: boundary layer height given by the ERA5 reanalysis (Online Resource section 2). Plain lines: vertical (boundary layer) and linear (free atmosphere) fits to estimate the stratification properties. **c–f:** Sketches representing the interaction between the giant dunes and the atmospheric flow for different meteorological conditions. **g:** Streamlines over a sinusoidal topography  $\xi(x, y)$  qualitatively representing the effect of low, medium and strong flow confinement, in relation to the above panels (see Appendix **4** for more details). The blue arrow indicates the undisturbed wind direction.

<sup>284</sup> et al. 2006; Jiang 2014):

$$\mathcal{F} = \frac{U}{\sqrt{\frac{\Delta\rho}{\rho_0} g H}}, \quad (1)$$

<sup>285</sup> where  $U$  is the wind velocity at the top of the ABL and  $\rho_0$  its average density.  
<sup>286</sup> The intensity of the stratification, i.e. the amplitude of the gradient  $|\partial_z \rho|$   
<sup>287</sup> in the FA, also impacts its-the ability to deform the capping layer under  
<sup>288</sup> the presence of an underlying obstacle, and thus affects the influence of flow  
<sup>289</sup> confinement. This can be quantified using the internal Froude number (Vosper  
<sup>290</sup> 2004; Stull 2006; Sheridan and Vosper 2006; Hunt et al. 2006; Jiang 2014)  
<sup>291</sup>  $\mathcal{F}_I = kU/N$ , where  $N = \sqrt{-g\partial_z \rho/\rho_0}$  is the Brunt-Väisälä frequency (Stull  
<sup>292</sup> 1988). Both Froude numbers have in practice the same qualitative effect on  
<sup>293</sup> flow confinement (a smaller Froude corresponding to a stiffer interface), and  
<sup>294</sup> we shall restrict the main discussion to  $\mathcal{F}$  only.

<sup>295</sup> With this theoretical framework in mind, and in the context of the mea-  
<sup>296</sup> sured wind data in the North and South Sand Sea stations, the smallest wind  
<sup>297</sup> disturbances are expected to occur during the day, when the ABL depth is the  
<sup>298</sup> largest and comparable to the dune wavelength ( $kH \gtrsim 1$ ), which corresponds  
<sup>299</sup> to a weak confinement situation (Fig. 47c,d). In contrast, large wind distur-  
<sup>300</sup> bances are expected to occur during the night, when the confinement is mainly  
<sup>301</sup> induced by a shallow ABL (Fig. 47e). However, this strong confinement can be  
<sup>302</sup> somewhat reduced in the case of strong winds, corresponding to large values of  
<sup>303</sup> the Froude number and a less ‘rigid’ interface (Fig. 47f). This is in qualitative  
<sup>304</sup> agreement with the transition from deflected to non-deflected winds related to  
<sup>305</sup> low and high velocities observed in our data (Sec. 2.2).

### <sup>306</sup> 3.2 Data distribution in the flow regimes

<sup>307</sup> We can go one step further and analyse how our data quantitatively spread  
<sup>308</sup> over the different regimes discussed above. For that purpose, one needs to  
<sup>309</sup> compute  $kH$  and  $\mathcal{F}$  from the time series.  $H$ ,  $U$  and the other atmospheric  
<sup>310</sup> parameters can be deduced from the various vertical profiles (temperature,  
<sup>311</sup> humidity) available in the ERA5 climate reanalysis (Online Resource section  
<sup>312</sup> 2). We quantify the flow deflection  $\delta_\theta$  as the minimal angle between the wind  
<sup>313</sup> orientations comparing the local measurements and the regional predictions.  
<sup>314</sup> We also compute the relative velocity modulation as

$$\delta_u = \frac{u_*^{\text{ERA}} - u_*^{\text{station}}}{u_*^{\text{ERA}}} \frac{u_*^{\text{ERA5-Land}} - u_*^{\text{Local mes.}}}{u_*^{\text{ERA5-Land}}}. \quad (2)$$

<sup>315</sup> These two quantities are represented as maps in the plane ( $\mathcal{F}$ ,  $kH$ ) (Fig. 58a,b),  
<sup>316</sup> and one can clearly identify different regions in these graphsplots. Small wind  
<sup>317</sup> disturbances (small  $\delta_\theta$  and  $\delta_u$ ) are located in the top-right part of the diagrams,  
<sup>318</sup> corresponding to a regime with low-interaction as well as low-confinement ( $kH$   
<sup>319</sup> and  $\mathcal{F}$  large enough, Fig. 47d). Lower values of  $kH$  (stronger interaction) or of

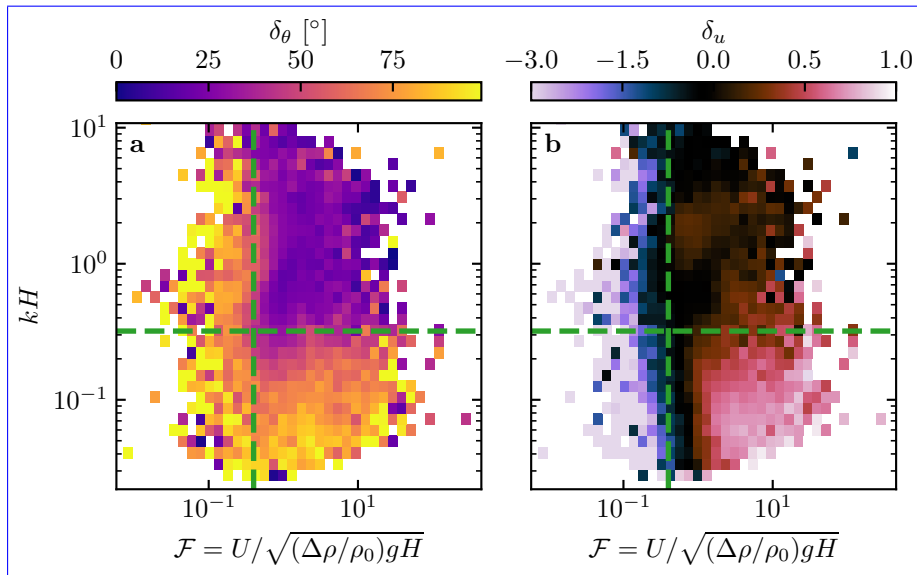


**Fig. 8** Regime diagrams of the wind deviation  $\delta_\theta$  **(a)** and relative attenuation/amplification  $\delta_u$  **(b)** in the space  $(\mathcal{F}, kH)$ , containing the data from both the North Sand Sea and South Sand Sea stations. **Green** The green dashed lines empirically delimit the different regimes. The point density in each bin of the diagrams is shown in Online Resource Fig. S14–S10 – 95% of the data occur in the range  $-1 < \delta u < 1$ . Similar regime diagrams in the spaces  $(\mathcal{F}_I, kH)$  and  $(\mathcal{F}_I, \mathcal{F})$  are shown in Online Resource Fig. S12–S11.

320 Froude number (stronger confinement) both lead to an increase in wind dis-  
 321 turbances, both in terms of orientation and velocity. Below a crossover value  
 322  $kH \simeq 0.3$ , wind disturbance is less sensitive to the  $\mathcal{F}$ -value. This is probably  
 323 due to enhanced non-linear effects linked to flow modulation by the obstacle  
 324 when confinement is strong (e.g. wakes and flow recirculations). The Froude  
 325 number also controls a transition from damped to amplified wind velocities  
 326 in the interdune, with a crossover around  $\mathcal{F} \simeq 0.4$  (Fig. 58b). Such an ampli-  
 327 fication is rather unexpected. Checking the occurrence of the corresponding  
 328 data, it appears that these amplifications are associated with the southerly  
 329 sea breeze, and occur dominantly during the October–March period, when the  
 330 other easterly wind is not present (Online Resource Fig. S12a–b). Further-  
 331 more, they occur less frequently during the afternoon, and more frequently at  
 332 the end of the day (Online Resource Fig. S12c). This effect may be linked  
 333 to a change in the flow behaviour in the lee side of the obstacles but further  
 334 measurements are needed in order to assess the different possibilities (Baines  
 335 1995; Vosper 2004).

336 As the hydrodynamic roughness  $z_0$  determine the magnitude of wind shear  
 337 velocities, Froude number  $\mathcal{F}$  and relative velocity modulation  $\delta_u$ , it is important  
 338 to discuss the sensitivity of the results to the  $z_0$ -values chosen for both the  
 339 ERA5-Land and the field data (see Online Resource section 4). Other quantities  
 340 associated with wind direction are independent of this choice. Considering

the possible range of realistic roughness values, the uncertainty on velocities estimated using the law of the wall is at most 30 %. A similar maximum uncertainty applies to the Froude number. This uncertainty also propagates to  $\delta_u$ , for which Figure S14 shows that the choice of roughness has little influence on its temporal variations even if it can induce a global increase or decrease of its values. Hence, the choice of the  $z_0$ -values will not qualitatively affect the overall aspect of the regime diagram presented in Figure 8b. It may only change the value of  $\delta_u$  for which the transition between regimes is observed (dashed green lines in Figure 8b). Our conclusions are thus robust with respect to the somewhat arbitrary choice of the hydrodynamic roughness values.

#### 351 4 Discussion and conclusion

The feedback of the giant dunes on the wind flow has important implications for smaller ~~seales~~ scale bedforms. As illustrated in Fig. 69, small linear dunes ( $\sim 50$  m wide) are often present ~~in~~ within the 1–2 km interdune spaces between giant linear dunes in the Namib Sand Sea (Livingstone et al. 2010). These smaller dunes do not exhibit the same orientation as the large ones, and are sometimes named ‘crossing dunes’ (Chandler et al. 2022). Whilst differences between large and small scale dune patterns are observed ubiquitously, they are ~~largely~~ usually attributed to the presence of two different dune growth mechanisms, leading to two different dune patterns (orientations and/or morphologies) for the same wind regime (Courrech du Pont et al. 2014; Runyon et al. 2017; Lü et al. 2017; Song et al. 2019; Gadal et al. 2020; Hu et al. 2021). Here, however, our arguments enable the development of differing orientations for the small and giant linear dunes ~~whilst also imposing governed by~~ the same dune growth mechanism (elongating mode). Figure 69 shows how the orientations for the small and giant dunes can be derived from the locally measured and regionally predicted winds respectively (red arrows in Fig. 69). These predictions require ~~a specification for~~ the threshold of ~~eolian sand transport~~ aeolian sand transport to be specified. Importantly, its value ~~expressed as~~ (a shear velocity  $u_{th} \approx 0.15 \text{ ms}^{-1}$  is reached in the deflected wind regime already estimated at  $u_{th} \approx 0.15 \text{ m s}^{-1}$  – see Appendix 4) can be reached in periods during which deflected winds are observed (recall that the stronger winds, responsible for most of the sediment transport and associated dune morphodynamics, are not deflected – see Fig. 6). The feedback of the giant dunes on the wind described in this study, through wind deflection and attenuation, thus provides a potential explanation for the existence of these small linear dunes elongating across the interdune, a dynamic which has remained unresolved to date. These crossing dunes could provide additional constraints for the inference of local winds from bedforms, similarly to that currently performed on Mars using ripple orientations (Liu and Zimbelman 2015; Hood et al. 2021). Further work is needed to investigate these processes in more detail, including measurements of sediment transport and flow on the top of dunes.

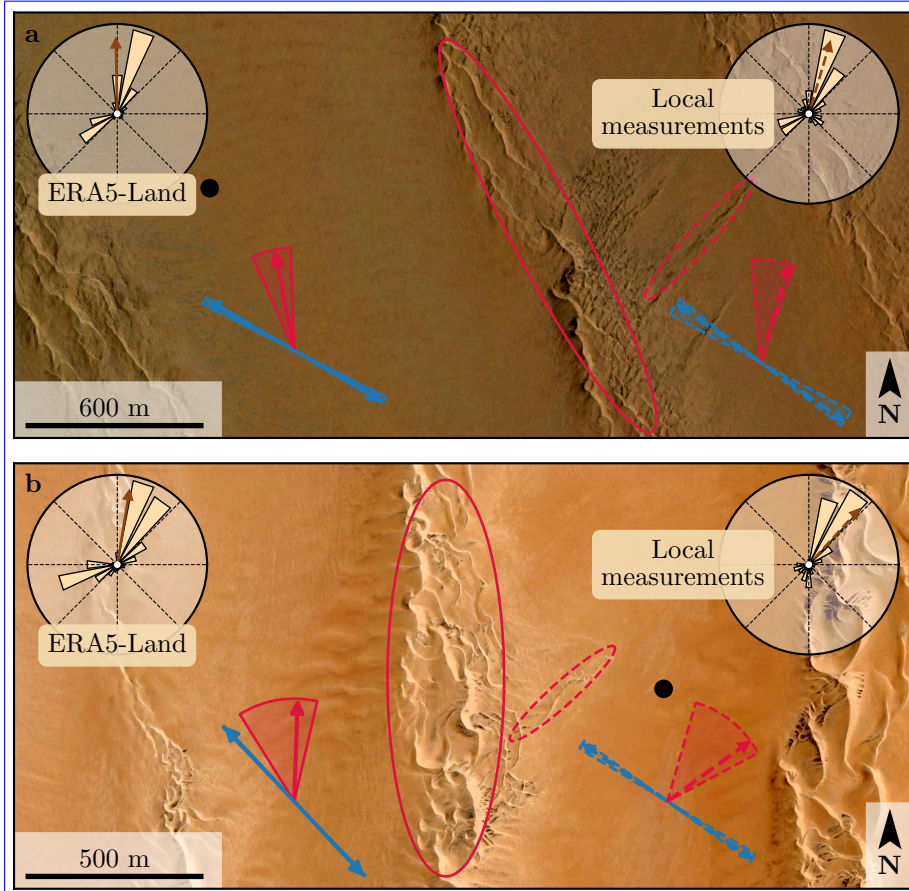


**Fig. 9** Implications for smaller scale patterns in (a) the South Sand Sea and (b) North Sand Sea. The ellipses indicate the different types of elongating dunes, at large (plain line) and small (dashed line) scales. Dune orientation are predicted using the model of Courrech du Pont et al. (2014) from the sand flux angular distributions, shown here (roses and along with the resultant transport direction (brown arrow) for typical values (grain size  $180 \mu\text{m}$ , flux-up ratio of 1.6). Code for corresponding arrows: use of ERA5-Land data (plain line), use of local measurements (dashed line), prediction for the bed instability growth mechanism (blue), prediction for the elongation growth mechanism (red). Wedges show the uncertainty on the orientation calculation when parameters are varied. The black dots indicate the location of the meteorological stations with respect to in the dunes interdune. See Appendix 2–4 for additional details.

This study presents the field and reanalysis-based evidence that wind flow patterns around giant dunes are influenced by the atmospheric boundary layer, particularly during nocturnal conditions. It leaves However, we do not address here the question of the limitation of the giant dune pattern coarsening, and leave open the debate as to whether the size of giant dunes is limited their size is controlled by the depth of this layer (Andreotti et al. 2009), in contrast

390 to ~~an unconstrained dune growth, sediment supply limited and~~ ever-slower  
391 ~~with size (?)~~ growth with size (Werner and Kocurek 1999; Gunn et al. 2022).  
392 More field evidence is ~~definitively~~ needed from additional dune fields, but this  
393 mechanism would ~~then~~ allow for the inference of the ABL depth from giant  
394 bedform wavelengths where measurements are not feasible or available, such  
395 as Titan (Lorenz et al. 2010).

396 To conclude on conditions under which the ERA5-Land reanalysis data can  
397 reliably be used to study dune morphodynamics, we summarise the compari-  
398 son of local (direct measurements) and regional (climate reanalysis) wind data  
399 ~~as follows~~. In flat areas, the agreement between the two confirms the ability of  
400 the ERA5-Land climate reanalysis to predict the wind regime down to scales  
401  $\sim 10$  km, i.e. the model grid. When smaller scale topographies are present  
402 (giant dunes in our case), locally measured winds can significantly differ from  
403 the regionally predicted ones. This is the case when the disturbances induced  
404 by the dunes interact with the lower part of the ABL vertical structure, which  
405 presents circadian variations. During the day, when the capping layer is typi-  
406 cally high, this interaction is small, and the ERA5-Land predictions are also  
407 quantitatively consistent with the local data. During the night, however, the  
408 presence of a shallow atmospheric boundary layer induces a strong confine-  
409 ment of the flow, and is associated with large wind deflection by the dunes.  
410 Importantly, we find that this effect can be counterbalanced for large wind  
411 velocities, which are capable of deforming the capping layer, thus decreasing  
412 the influence of the confinement.

413 The theoretical computation of the wind disturbances induced by sinu-  
414 soidal ridges under flow confinement has been performed in the linear limit  
415 (Andreotti et al. 2009, 2012), i.e. when the aspect ~~ration~~<sup>ratio</sup> of these ridges  
416 is small ( $k\xi_0 \ll 1$ ). These models are able to qualitatively reproduce the ob-  
417 served wind deflection (Appendix 4, Online Resource Figs. ?? and ??S11 and  
418 S13), and thus provide the physical support for the interpretation we propose  
419 here based on hydrodynamic regimes. However, these models cannot quanti-  
420 tatively predict the magnitude of ~~these~~<sup>our</sup> observations, probably due to the  
421 presence of expected non-linearities in high confinement situations linked to  
422 strong flow modulations. Besides, these linear calculations only predict wind  
423 attenuation in the interdune, in contrast with the observed enhanced veloc-  
424 ities associated with particular evening winds from the ~~South~~<sup>south</sup> during  
425 the period October–March (Online Resource Fig. ??S12). Some other models  
426 predict different spatial flow structures in response to a modulated topogra-  
427 phy, such as lee waves and rotors (Baines 1995; Vosper 2004). However, our  
428 measurements are located at a single point in the interdune, ~~so we are and we~~  
429 ~~are thus~~ unable to explore these types of responses. Data at different places  
430 along and across the ridges are needed to investigate and possibly map such  
431 flow structures, and for further comparisons with the models.

432 **Acknowledgements** We would like to acknowledge the contributors of the following open-  
433 source python libraries, Matplotlib (Hunter 2007), Numpy (Harris et al. 2020) and Scipy

434 (Virtanen et al. 2020), which provide an incredibly efficient ecosystem allowing scientific  
435 research in Python. We also thank B. Andreotti and A. Gunn for useful discussions.

436 All data used in this study can be found in Gadal et al. (2022). Note that it contains  
437 modified Copernicus Climate Change Service Information (2021). Neither the European  
438 Commission nor ECMWF is responsible for any use that may be made of the Copernicus  
439 Information or Data it contains. Fully documented codes used  
440 Documented codes used in this study to analyse this study-data are available at <https://github.com/Cgadal/GiantDunes>  
441 (will be made public upon acceptance of this manuscript for publication).

442 Multiple grants have supported the collection of wind data through visits to the four  
443 sites between 2013 and 2020 (John Fell Oxford University Press (OUP) Research Fund  
444 (121/474); National Geographic (CP-029R-17); Natural Environment Research Council UK  
445 (NE/R010196/1 and NE/H021841/1 NSFGEONERC); Southampton Marine and Maritime  
446 Institute SMMI EPSRC-GCRF UK), along with research permits (1978/2014, 2140/2016,  
447 2304/2017, 2308/2017, RPIV00022018, RPIV0052018, RPIV00230218). The authors are  
448 very grateful for support from Etosha National Park (especially Shyane Kötting, Boas Erckie,  
449 Pierre du Preez, Claudine Cloete, Immanuel Kapofi, Wilferd Versfeld, and Werner Kilian),  
450 Gobabeb Namib Research Institute (Gillian Maggs-Kölling, Maggs-Kölling and Eugene Marais),  
451 The Skeleton Coast National Park (Joshua Kazeurua). Various researchers and desert enthusiasts  
452 have assisted with instruments and the logistics of expeditions, especially Mary Seely for expert  
453 guidance at the North Sand Sea site.

454 Finally, we acknowledge financial support from the Laboratoire d'Excellence UnivEarthS  
455 Grant ANR-10-LABX-0023, the Initiative d'Excellence Université de  
456 Paris Grant ANR-18-IDEX-0001, the French National Research Agency Grants ANR-17-  
457 CE01-0014/SONO and the National Science Center of Poland Grant 2016/23/B/ST10/01700.

## 458 Appendix 1: Linear theory of wind response to topographic perturbation

460 Following the work of Fourrière et al. (2010), Andreotti et al. (2012) and  
461 Andreotti et al. (2009), we briefly describe in this appendix the framework  
462 for the linear response of a turbulent flow to a topographic perturbation of  
463 small aspect ratio. As a general bed elevation can be decomposed into Fourier  
464 modes, we focus here on a sinusoidal topography:

$$\xi = \xi_0 \cos [k (\cos(\alpha)y - \sin(\alpha)x)], \quad (3)$$

465 which is also a good approximation for the giant dunes observed in the North  
466 Sand Sea and South Sand Sea Station (Fig. 12 and Online Resource Fig. S5S4).  
467 Here,  $x$  and  $y$  are the streamwise and spanwise coordinates,  $k = 2\pi/\lambda$  the  
468 wavenumber of the sinusoidal perturbation,  $\alpha$  its crest orientation with respect  
469 to the  $x$ -direction (anticlockwise) and  $\xi_0$  its amplitude. The two components  
470 of the basal shear stress  $\tau = \rho_0 u_* \mathbf{u}_*$ , constant in the flat bottom reference  
471 case, can then be generically written as:

$$\tau_x = \tau_0 \left( 1 + k \xi_0 \sqrt{\mathcal{A}_x^2 + \mathcal{B}_x^2} \cos [k (\cos(\alpha)y - \sin(\alpha)x) + \phi_x] \right), \quad (4)$$

$$\tau_y = \tau_0 k \xi_0 \sqrt{\mathcal{A}_y^2 + \mathcal{B}_y^2} \cos [k (\cos(\alpha)y - \sin(\alpha)x) + \phi_y], \quad (5)$$

472 where  $\tau_0$  is the reference basal shear stress on a flat bed. We have defined  
473 the phase  $\phi_{x,y} = \tan^{-1}(\mathcal{B}_{x,y}/\mathcal{A}_{x,y})$  from the in-phase and in-quadrature hy-  
474 drodynamical coefficients  $\mathcal{A}_{x,y}$  and  $\mathcal{B}_{x,y}$ . They are functions of  $k$  and of the

475 flow conditions, i.e the bottom roughness, the vertical flow structure and the  
 476 incident flow direction, and the theoretical framework developed in the above  
 477 cited papers proposes methods to compute them in the linear regime.

478 Following Andreotti et al. (2012), the effect of the incident wind direction  
 479 can be approximated by the following expressions:

$$\mathcal{A}_x = \mathcal{A}_0 \sin^2 \alpha, \quad (6)$$

$$\mathcal{B}_x = \mathcal{B}_0 \sin^2 \alpha, \quad (7)$$

$$\mathcal{A}_y = -\frac{1}{2} \mathcal{A}_0 \cos \alpha \sin \alpha, \quad (8)$$

$$\mathcal{B}_y = -\frac{1}{2} \mathcal{B}_0 \cos \alpha \sin \alpha, \quad (9)$$

480 where  $\mathcal{A}_0$  and  $\mathcal{B}_0$  are now two coefficients independent of the dune orientation  
 481  $\alpha$ , corresponding to the transverse case ( $\alpha = 90^\circ$ ). ~~For~~ In the case of a fully  
 482 turbulent boundary layer capped by a stratified atmosphere, these coefficients  
 483 depend on  $kH$ ,  $kz_0$ ,  $\mathcal{F}$  and  $\mathcal{F}_I$  (Andreotti et al. 2009). ~~In this study~~ For their  
 484 computation, we assume here a constant hydrodynamic roughness  $z_0 \simeq 1$  mm  
 485 (Online Resource section 1). For the considered giant dunes, this leads to  
 486  $kz_0 \simeq 2 \cdot 10^{-6}$ , as their wavelength is  $\lambda \simeq 2.4$  km (or  $k \simeq 2 \cdot 10^{-3} \text{ m}^{-1}$ ). Values  
 487 of  $z_0$  extracted from field data indeed typically fall between 0.1 mm and 10  
 488 mm (Sherman and Farrell 2008; Field and Pelletier 2018). Importantly,  $\mathcal{A}_0$   
 489 and  $\mathcal{B}_0$  do not vary much in the corresponding range of  $kz_0$  (Fourrière et al.  
 490 2010), and the results presented here are robust with respect to this choice.

491 With capping layer height and Froude numbers computed from the ERA5-  
 492 Land time series, the corresponding  $\mathcal{A}_0$  and  $\mathcal{B}_0$  can be deduced, as displayed  
 493 in Online Resource Fig. ??S13. Interestingly, it shows similar regimes as in  
 494 the diagrams of Fig. ??S13 and Online Resource Fig. ??S11a,b, supporting the  
 495 underlying physics. However, the agreement is qualitative only. Further, the  
 496 linearity assumption of the theoretical framework requires  $(|\tau| - \tau_0) / \tau_0 \ll 1$ ,  
 497 which translates into  $k\xi \sqrt{\mathcal{A}_0^2 + \mathcal{B}_0^2} \ll 1$ . In our case, the giant dune morphol-  
 498 ogy gives  $k\xi_0 \simeq 0.1$ , which means that one quits the regime of validity of the  
 499 linear theory when the coefficient modulus  $\sqrt{\mathcal{A}_0^2 + \mathcal{B}_0^2}$  becomes larger than a  
 500 few units. In accordance with the theoretical expectations, these coefficients  
 501 present values on the order of unity ( $\mathcal{A}_0 \simeq 3$  and  $\mathcal{B}_0 \simeq 1$ ) in unconfined situa-  
 502 tions (Claudin et al. 2013; Lü et al. 2021). In contrast and as illustrated in  
 503 Online Resource Fig. ??S13a,b, larger values are predicted in case of strong  
 504 confinement, which does not allow us to proceed to further quantitative com-  
 505 parison with the data.

506 Finally, the linear model is also able to reproduce the enhancement of  
 507 the flow deflection over the sinusoidal ridges when  $\sqrt{\mathcal{A}_0^2 + \mathcal{B}_0^2}$  is increased  
 508 (Online Resource Fig. ??S13). Here, using  $k\xi_0 \simeq 0.1$  to be representative of  
 509 the amplitude of the giant dunes at the North Sand Sea station, the coefficient  
 510 modulus is bounded to 10.

511 **Appendix 2: Sediment transport and dune morphodynamics**

512 We summarise in this appendix the sediment transport and dune morphodynamics theoretical framework leading to the prediction of sand fluxes and dune orientations from wind data.

515 *Sediment transport* — The prediction of sand fluxes from wind data has been  
 516 a long standing issue in aeolian geomorphological studies (Fryberger and Dean  
 517 1979; Pearce and Walker 2005; Sherman and Li 2012; Shen et al. 2019). Based  
 518 on laboratory studies in wind tunnels (Rasmussen et al. 1996; Iversen and  
 519 Rasmussen 1999; Creyssels et al. 2009; Ho et al. 2011), as well as physical  
 520 considerations (Ungar and Haff 1987; Andreotti 2004; Durán et al. 2011; Pähzt  
 521 and Durán 2020), it has been shown that the steady saturated saltation flux  
 522 over a flat sand bed depends linearly on the shear stress:

$$\frac{q_{\text{sat}}}{Q} = \Omega \sqrt{\Theta_{\text{th}}} (\Theta - \Theta_{\text{th}}), \quad (10)$$

523 where  $\Omega$  is a proportionality constant,  $Q = d\sqrt{(\rho_s - \rho_0)gd/\rho_0}$  is a characteristic flux,  
 524  $\Theta = \rho_0 u_*^2 / (\rho_s - \rho_0)gd$  the Shields number, and  $\Theta_{\text{th}}$  its threshold value below which saltation vanishes.  $\rho_s = 2.6 \text{ g cm}^{-3}$  and  $d = 180 \mu\text{m}$  are  
 525 the grain density and diameter, and  $g$  is the gravitational acceleration. The shear velocity, and consequently the Shields number as well as the sediment flux, are time dependent.

529 Recently, Pähzt and Durán (2020) suggested an additional quadratic term  
 530 in Shields to account for grain-grain interactions within the transport layer at  
 531 strong wind velocities:

$$\frac{q_{\text{sat}, t}}{Q} = \frac{2\sqrt{\Theta_{\text{th}}}}{\kappa\mu} (\Theta - \Theta_{\text{th}}) \left( 1 + \frac{C_M}{\mu} [\Theta - \Theta_{\text{th}}] \right), \quad (11)$$

532 where  $\kappa = 0.4$  is the von Kármán constant,  $C_M \simeq 1.7$  a constant and  $\mu \simeq 0.6$  is  
 533 a friction coefficient, taken to be the avalanche slope of the granular material.  
 534 The fit of this law to the experimental data of Creyssels et al. (2009) and  
 535 Ho et al. (2011) gives  $\Theta_{\text{th}} = 0.0035$ . The fit of Eq. 10 on these same data  
 536 similarly gives  $\Omega \simeq 8$  and  $\Theta_{\text{th}} = 0.005$ . The sand flux angular distributions  
 537 and the dune orientations in Fig. 6–9 are calculated using this law (11). We  
 538 have checked that using the ordinary linear relationship (10) instead does not  
 539 change the predicted dune orientations by more than a few degrees.

540 *Dune orientations* — Dune orientations are predicted with the dimensional model of Courrech du Pont et al. (2014), from the sand flux time series computed with the above transport law. Two orientations are possible depending on the mechanism dominating the dune growth: elongation or bed instability. The orientation  $\alpha$  corresponding to the bed instability is then the one that maximises the following growth rate (Rubin and Hunter 1987):

$$\sigma \propto \frac{1}{H_d W_d T} \int_0^T q_{\text{crest}} |\sin(\theta - \alpha)| dt, \quad (12)$$

546 where  $\theta$  is the wind orientation measured with respect to the same reference  
 547 as  $\alpha$ , and  $H_d$  and  $W_d$  are dimensional constants respectively representing the  
 548 dune height and width. The integral runs over a time  $T$ , which must be repre-  
 549 sentative of the characteristic period of the wind regime. The flux at the crest  
 550 is expressed as:

$$q_{\text{crest}} = q_{\text{sat}} [1 + \gamma |\sin(\theta - \alpha)|], \quad (13)$$

551 where the flux-up ratio  $\gamma$  has been calibrated to 1.6 using field studies, under-  
 552 water laboratory experiments and numerical simulations. Predictions of the  
 553 linear analysis of Gadal et al. (2019) and Delorme et al. (2020) give similar  
 554 results.

555 Similarly, the dune orientation corresponding to the elongation mechanism  
 556 is the one that verifies:

$$\tan(\alpha) = \frac{\langle q_{\text{crest}}(\alpha) \mathbf{e}_\theta \rangle \cdot \mathbf{e}_{WE}}{\langle q_{\text{crest}}(\alpha) \mathbf{e}_\theta \rangle \cdot \mathbf{e}_{SN}}, \quad (14)$$

557 where  $\langle \cdot \rangle$  denotes a vectorial time average. The unitary vectors  $\mathbf{e}_{WE}$ ,  $\mathbf{e}_{SN}$  and  
 558  $\mathbf{e}_\theta$  are in the West-East, South-North and wind directions, respectively.

559 The resulting computed dune orientations, blue and red arrows in Fig. 69,  
 560 then depend on a certain number of parameters (grain properties, flux-up ratio,  
 561 etc.), for which we take typical values for aeolian sandy deserts. Due to the lack  
 562 of measurements in the studied places, some uncertainties can be expected. We  
 563 therefore run a sensitivity test by calculating the dune orientations for grain  
 564 diameters ranging from 100  $\mu\text{m}$  to 400  $\mu\text{m}$  and for a speed-up ratio between  
 565 0.1 and 10 (wedges in Fig. 69).

**566 References**

- 567 Andreotti B (2004) A two-species model of aeolian sand transport. *J Fluid  
568 Mech* 510:47–70
- 569 Andreotti B, Claudin P, Douady S (2002) Selection of dune shapes and veloc-  
570 ities part 1: Dynamics of sand, wind and barchans. *The European Physical  
571 Journal B-Condensed Matter and Complex Systems* 28:321–339
- 572 Andreotti B, Fourrière A, Ould-Kaddour F, Murray B, Claudin P (2009) Gi-  
573 ant aeolian dune size determined by the average depth of the atmospheric  
574 boundary layer. *Nature* 457:1120–1123
- 575 Andreotti B, Claudin P, Devauchelle O, Durán O, Fourrière A (2012) Bedforms  
576 in a turbulent stream: ripples, chevrons and antidunes. *J Fluid Mech* 690:94–  
577 128
- 578 Ashkenazy Y, Yizhaq H, Tsoar H (2012) Sand dune mobility under climate  
579 change in the kalahari and australian deserts. *Climatic Change* 112:901–923
- 580 Baddock M, Livingstone I, Wiggs G (2007) The geomorphological significance  
581 of airflow patterns in transverse dune interdunes. *Geomorphology* 87:322–  
582 336
- 583 Bagnold RA (1941) *The Physics of Blown Sand and Desert Dunes*. London :  
584 Methuen : Chapman & Hall
- 585 Baines PG (1995) Topographic effects in stratified flows. Cambridge university  
586 press
- 587 Bauer BO, Sherman DJ, Wolcott JF (1992) Sources of uncertainty in shear  
588 stress and roughness length estimates derived from velocity profiles. *The  
589 Professional Geographer* 44:453–464
- 590 Belcher S, Hunt J (1998) Turbulent flow over hills and waves. *Annu Rev Fluid  
591 Mech* 30:507–538
- 592 Blumberg DG, Greeley R (1996) A comparison of general circulation model  
593 predictions to sand drift and dune orientations. *J Clim* 9:3248–3259
- 594 Bristow NR, Best J, Wiggs GFS, Nield JM, Baddock MC, Delorme P, Chris-  
595 tensen KT (2022) Topographic perturbation of turbulent boundary layers  
596 by low-angle, early-stage aeolian dunes. *Earth Surf Process Landf* n/a, DOI  
597 <https://doi.org/10.1002/esp.5326>
- 598 Brookfield M (1977) The origin of bounding surfaces in ancient aeolian sand-  
599 stones. *Sedimentology* 24:303–332
- 600 Brown S, Nickling WG, Gillies JA (2008) A wind tunnel examination of shear  
601 stress partitioning for an assortment of surface roughness distributions. *J  
602 Geophys Res* 113:F02S06
- 603 Chandler C, Radebaugh J, McBride J, Morris T, Narteau C, Arnold K, Lorenz  
604 R, Barnes J, Hayes A, Rodriguez S, Rittenour T (2022) Near-surface struc-  
605 ture of a large linear dune and an associated crossing dune of the northern  
606 Namib Sand Sea from ground penetrating radar: Implications for the his-  
607 tory of large linear dunes on Earth and Titan. *Aeolian Research* 57:100813,  
608 DOI <https://doi.org/10.1016/j.aeolia.2022.100813>
- 609 Chang H, Simons D (1970) The bed configuration of straight sand-bed channels  
610 when flow is nearly critical. *J Fluid Mech* 42:491–495

- 611 Charru F, Andreotti B, Claudin P (2013) Sand ripples and dunes. *Annu Rev  
612 Fluid Mech* 45:469–493
- 613 Claudin P, Wiggs G, Andreotti B (2013) Field evidence for the upwind velocity  
614 shift at the crest of low dunes. *Boundary-Layer Meteorol* 148:195–206
- 615 Claudin P, Durán O, Andreotti B (2017) Dissolution instability and roughen-  
616 ing transition. *J Fluid Mech* 832:R2
- 617 Claudin P, Louge M, Andreotti B (2021) Basal pressure variations induced by  
618 a turbulent flow over a wavy surface. *Frontiers in Physics* 9:682564
- 619 Colombini M (2004) Revisiting the linear theory of sand dune formation. *J  
620 Fluid Mech* 502:1–16
- 621 Courrech du Pont S (2015) Dune morphodynamics. *C R Phys* 16:118–138
- 622 Courrech du Pont S, Narteau C, Gao X (2014) Two modes for dune orientation.  
623 *Geology* 42:743–746
- 624 Creyssels M, Dupont P, El Moctar AO, Valance A, Cantat I, Jenkins JT, Pasini  
625 JM, Rasmussen KR (2009) Saltating particles in a turbulent boundary layer:  
626 experiment and theory. *J Fluid Mech* 625:47–74
- 627 de Winter W, Donker J, Sterk G, Van Beem J, Ruessink G (2020) Regional  
628 versus local wind speed and direction at a narrow beach with a high and  
629 steep foredune. *Plos one* 15:e0226983
- 630 Dee DP, Uppala SM, Simmons AJ, Berrisford P, Poli P, Kobayashi S, Andrae  
631 U, Balmaseda M, Balsamo G, Bauer dP, et al. (2011) The ERA-Interim  
632 reanalysis: Configuration and performance of the data assimilation system.  
633 *Q J R Meteorol Soc* 137:553–597
- 634 Delorme P, Wiggs G, Baddock M, Claudin P, Nield J, Valdez A (2020) Dune  
635 initiation in a bimodal wind regime. *J Geophys Res* 125:e2020JF005757
- 636 Durán O, Claudin P, Andreotti B (2011) On aeolian transport: Grain-scale  
637 interactions, dynamical mechanisms and scaling laws. *Aeolian Res* 3:243–  
638 270
- 639 Durran DR (1990) Mountain waves and downslope winds. In: *Atmospheric  
640 processes over complex terrain*, Springer, pp 59–81
- 641 Dyer A (1974) A review of flux-profile relationships. *Boundary-Layer Meteorol*  
642 7:363–372
- 643 Ewing RC, Kocurek G, Lake LW (2006) Pattern analysis of dune-field param-  
644 eters. *Earth Surf Process Landf* 31:1176–1191
- 645 Farr TG, Rosen PA, Caro E, Crippen R, Duren R, Hensley S, Kobrick M,  
646 Paller M, Rodriguez E, Roth L, et al. (2007) The shuttle radar topography  
647 mission. *Rev Geophys* 45
- 648 Fernando H, Mann J, Palma J, Lundquist JK, Barthelmie RJ, Belo-Pereira M,  
649 Brown W, Chow F, Gerz T, Hocut C, et al. (2019) The perdigão: Peering  
650 into microscale details of mountain winds. *Bull Am Meteorol Soc* 100:799–  
651 819
- 652 Field JP, Pelletier JD (2018) Controls on the aerodynamic roughness length  
653 and the grain-size dependence of aeolian sediment transport. *Earth Surf  
654 Process Landf* 43:2616–2626
- 655 Finnigan J, Raupach M, Bradley E, Aldis G (1990) A wind tunnel study  
656 of turbulent flow over a two-dimensional ridge. *Boundary-Layer Meteorol*

- 657 50:277–317
- 658 Finnigan J, Ayotte K, Harman I, Katul G, Oldroyd H, Patton E, Poggi D,  
659 Ross A, Taylor P (2020) Boundary-layer flow over complex topography.  
Boundary-Layer Meteorol 177:247–313
- 660 Flack K, Schultz M (2010) Review of hydraulic roughness scales in the fully  
661 rough regime. Journal of Fluids Engineering 132:041203
- 662 Fourrière A, Claudin P, Andreotti B (2010) Bedforms in a turbulent stream:  
663 formation of ripples by primary linear instability and of dunes by nonlinear  
664 pattern coarsening. J Fluid Mech 649:287–328
- 665 Frederick KA, Hanratty TJ (1988) Velocity measurements for a turbulent non-  
666 separated flow over solid waves. Exp Fluids 6:477–486
- 667 Fryberger SG, Dean G (1979) Dune forms and wind regime. A study of global  
668 sand seas 1052:137–169
- 669 Gadal C, Narteau C, Courrech Du Pont S, Rozier O, Claudin P (2019) Incip-  
670 ient bedforms in a bidirectional wind regime. J Fluid Mech 862:490–516
- 671 Gadal C, Narteau C, Courrech du Pont S, Rozier O, Claudin P (2020) Peri-  
672 odicity in fields of elongating dunes. Geology 48:343–347
- 673 Gadal C, Delorme P, Narteau C, Wiggs G, Baddock M, Nield JM, Claudin  
674 P (2022) Data used in 'Local wind regime induced by giant linear dunes:  
675 comparison of ERA5-Land re-analysis with surface measurements'. DOI  
676 10.5281/zenodo.6343138
- 677 Gao X, Narteau C, Gadal C (2021) Migration of reversing dunes against the  
678 sand flow path as a singular expression of the speed-up effect. Journal of  
679 Geophysical Research: Earth Surface 126(5):e2020JF005913
- 680 Garratt JR (1994) The atmospheric boundary layer. Earth-Science Reviews  
681 37:89–134
- 682 Garvey B, Castro IP, Wiggs G, Bullard J (2005) Measurements of flows over  
683 isolated valleys. Boundary-Layer Meteorol 117:417–446
- 684 Gong W, Ibbetson A (1989) A wind tunnel study of turbulent flow over model  
685 hills. Boundary-Layer Meteorol 49:113–148
- 686 Gong W, Taylor P, Dörnbrack A (1996) Turbulent boundary-layer flow over  
687 fixed aerodynamically rough two-dimensional sinusoidal waves. J Fluid Mech  
688 312:1–37
- 689 Guérin A, Derr J, Du Pont SC, Berhanu M (2020) Streamwise dissolution  
690 patterns created by a flowing water film. Phys Rev Lett 125:194502
- 691 Gunn A, Wanker M, Lancaster N, Edmonds D, Ewing R, Jerolmack  
692 D (2021) Circadian rhythm of dune-field activity. Geophys Res Lett  
693 48:e2020GL090924
- 694 Gunn A, Casasanta G, Di Liberto L, Falcini F, Lancaster N, Jerolmack DJ  
695 (2022) What sets aeolian dune height? Nature communications 13(1):1–8
- 696 Harris CR, Millman KJ, van der Walt SJ, Gommers R, Virtanen P, Cournapeau  
697 D, Wieser E, Taylor J, Berg S, Smith NJ, et al. (2020) Array program-  
698 ming with numpy. Nature 585:357–362
- 699 Havholm KG, Kocurek G (1988) A preliminary study of the dynamics of  
700 a modern draa, Algodones, southeastern California, USA. Sedimentology  
701 35:649–669

- 703 Hersbach H, Bell B, Berrisford P, Hirahara S, Horányi A, Muñoz-Sabater J,  
704 Nicolas J, Peubey C, Radu R, Schepers D, et al. (2020) The ERA5 global  
705 reanalysis. *Q J R Meteorol Soc* 146:1999–2049
- 706 Hesp P, Illenberger W, Rust I, McLachlan A, Hyde R (1989) Some aspects of  
707 transgressive dunefield and transverse dune geomorphology and dynamics,  
708 south coast, South Africa. *Zeitschrift fur Geomorphologie*, Supplementband  
709 73:111–123
- 710 Hesp PA, Hastings K (1998) Width, height and slope relationships and aero-  
711 dynamic maintenance of barchans. *Geomorphology* 22:193–204
- 712 Hesp PA, Smyth TAG, Nielsen P, Walker IJ, Bauer BO, Davidson-Arnott R  
713 (2015) Flow deflection over a foredune. *Geomorphology* 230:64–74
- 714 Ho TD, Valance A, Dupont P, Ould El Moctar A (2011) Scaling laws in aeolian  
715 sand transport. *Phys Rev Lett* 106:4–7
- 716 Hood DR, Ewing RC, Roback KP, Runyon K, Avouac JP, McEnroe M (2021)  
717 Inferring airflow across martian dunes from ripple patterns and dynamics.  
718 *Frontiers in Earth Science* 9:702828
- 719 Howard AD (1977) Effect of slope on the threshold of motion and its applica-  
720 tion to orientation of wind ripples. *Geological Society of America Bulletin*  
721 88:853–856
- 722 Hu Z, Gao X, Lei J, Zhou N (2021) Geomorphology of aeolian dunes in the  
723 western Sahara Desert. *Geomorphology* 392:107916
- 724 Hunt J, Leibovich S, Richards K (1988) Turbulent shear flows over low hills.  
725 *Q J R Meteorol Soc* 114:1435–1470
- 726 Hunt JCR, Vilenski GG, Johnson ER (2006) Stratified separated flow around  
727 a mountain with an inversion layer below the mountain top. *J Fluid Mech*  
728 556:105–119
- 729 Hunter JD (2007) Matplotlib: A 2d graphics environment. *Computing in sci-  
730 ence & engineering* 9:90–95
- 731 Hunter RE, Richmond BM, Alpha TR (1983) Storm-controlled oblique dunes  
732 of the Oregon coast. *Geol Soc America Bull* 94:1450–1465
- 733 Iversen JD, Rasmussen KR (1999) The effect of wind speed and bed slope on  
734 sand transport. *Sedimentology* 46:723–731
- 735 Jackson PS, Hunt JCR (1975) Turbulent wind flow over a low hill. *Q J R  
736 Meteorol Soc* 101:929–955
- 737 Jiang Q (2014) Applicability of reduced-gravity shallow-water theory to atmo-  
738 spheric flow over topography. *J Atmos Sci* 71:1460–1479
- 739 Jolivet M, Braucher R, Dovchintseren D, Hocquet S, Schmitt J, ASTER Team  
740 (2021) Erosion around a large-scale topographic high in a semi-arid sedimen-  
741 tary basin: Interactions between fluvial erosion, aeolian erosion and aeolian  
742 transport. *Geomorphology* 386:107747
- 743 Kennedy JF (1963) The mechanics of dunes and antidunes in erodible-bed  
744 channels. *J Fluid Mech* 16:521–544
- 745 Kim HG, Patel VC, Lee CM (2000) Numerical simulation of wind flow over  
746 hilly terrain. *J Wind Eng Ind Aerodyn* 87:45–60
- 747 Kroy K, Sauermann G, Herrmann HJ (2002) Minimal model for aeolian sand  
748 dunes. *Phys Rev E* 66:031302

- 749 Lancaster J, Lancaster N, Seely M (1984) Climate of the central Namib desert.  
750 Madoqua 1984:5–61
- 751 Lancaster N (1985) Winds and sand movements in the Namib sand sea. *Earth  
752 Surf Process Landf* 10:607–619
- 753 Lancaster N, Nickling W, Neuman CM, Wyatt V (1996) Sediment flux and  
754 airflow on the stoss slope of a barchan dune. *Geomorphology* 17:55–62
- 755 Lewis HW, Mobbs SD, Lehning M (2008) Observations of cross-ridge flows  
756 across steep terrain. *Q J R Meteorol Soc* 134:801–816
- 757 Liu ZYC, Zimbelman JR (2015) Recent near-surface wind directions inferred  
758 from mapping sand ripples on martian dunes. *Icarus* 261:169–181
- 759 Livingstone I, Warren A (2019) Aeolian geomorphology: a new introduction.  
760 Wiley
- 761 Livingstone I, Bristow C, Bryant RG, Bullard J, White K, Wiggs GFS, Baas  
762 ACW, Bateman MD, Thomas DSG (2010) The Namib Sand Sea digital  
763 database of aeolian dunes and key forcing variables. *Aeolian Res* 2:93–104
- 764 Lorenz R, Claudin P, Andreotti B, Radebaugh J, Tokano T (2010) A 3 km at-  
765 mospheric boundary layer on Titan indicated by dune spacing and Huygens  
766 data. *Icarus* 205:719–721
- 767 Lü P, Narteau C, Dong Z, Rozier O, Du Pont SC (2017) Unravelling raked  
768 linear dunes to explain the coexistence of bedforms in complex dunefields.  
769 *Nature Communications* 8:1–9
- 770 Lü P, Narteau C, Dong Z, Claudin P, Rodriguez S, An Z, Fernandez-Cascales  
771 L, Gadal C, Courrech du Pont S (2021) Direct validation of dune instability  
772 theory. *Proceedings of the National Academy of Sciences* 118
- 773 Mason P, Sykes R (1979) Flow over an isolated hill of moderate slope. *Q J R  
774 Meteorol Soc* 105:383–395
- 775 McKenna Neuman C, Lancaster N, Nickling WG (1997) Relations between  
776 dune morphology, air flow, and sediment flux on reversing dunes, Silver Peak,  
777 Nevada. *Sedimentology* 44:1103–1111, DOI 10.1046/j.1365-3091.1997.d01-  
778 61.x
- 779 Mizumura K (1995) Free-surface profile of open-channel flow with wavy bound-  
780 ary. *J Hydraul Eng* 121:533–539
- 781 Monin AS, Obukhov AM (1954) Basic laws of turbulent mixing in the surface  
782 layer of the atmosphere. *Contrib Geophys Inst Acad Sci USSR* 151:e187
- 783 Mulligan KR (1988) Velocity profiles measured on the windward slope of a  
784 transverse dune. *Earth Surf Process Landf* 13:573–582
- 785 Muñoz-Sabater J, Dutra E, Agustí-Panareda A, Albergel C, Arduini G, Bal-  
786 samo G, Boussetta S, Choulga M, Harrigan S, Hersbach H, et al. (2021)  
787 ERA5-Land: A state-of-the-art global reanalysis dataset for land applica-  
788 tions. *Earth Syst Sci Data* 13:4349–4383
- 789 Nield JM, King J, Wiggs GFS, Leyland J, Bryant RG, Chiverrell RC, Darby  
790 SE, Eckhardt FD, Thomas DSG, Vircavs LH, Washington R (2014) Esti-  
791 mating aerodynamic roughness over complex surface terrain. *J Geophys Res*  
792 118:12948–12961
- 793 Nield JM, Wiggs GG, Baddock MC, Hipondoka MH (2017) Coupling lee-  
794 side rainfall to avalanche characteristics in aeolian dune dynamics. *Geology*

- 795 45:271–274
- 796 Pähzt T, Durán O (2020) Unification of aeolian and fluvial sediment transport  
797 rate from granular physics. *Phys Rev Lett* 124:168001
- 798 Pearce KI, Walker IJ (2005) Frequency and magnitude biases in the 'Fryberger'  
799 model, with implications for characterizing geomorphically effective winds.  
800 *Geomorphology* 68:39–55
- 801 Pelletier JD, Field JP (2016) Predicting the roughness length of turbulent flows  
802 over landscapes with multi-scale microtopography. *Earth Surface Dynamics*  
803 4:391–405
- 804 Poggi D, Katul G, Albertson J, Ridolfi L (2007) An experimental investigation  
805 of turbulent flows over a hilly surface. *Phys Fluids* 19:036601
- 806 Rasmussen KR (1989) Some aspects of flow over coastal dunes. *Proceedings of*  
807 *the Royal Society of Edinburgh, Section B: Biological Sciences* 96:129–147
- 808 Rasmussen KR, Iversen JD, Rautaheimo P (1996) Saltation and wind flow  
809 interaction in a variable slope wind tunnel. *Geomorphology* 17:19–28
- 810 Raupach M (1992) Drag and drag partition on rough surfaces. *Boundary-Layer*  
811 *Meteorol* 60:375–395
- 812 Rozier O, Narteau C, Gadal C, Claudin P, Courrech du Pont S (2019)  
813 Elongation and stability of a linear dune. *Geophysical Research Letters*  
814 46(24):14521–14530
- 815 Rubin DM, Hunter RE (1987) Bedform alignment in directionally varying  
816 flows. *Science* 237:276–278
- 817 Runyon K, Bridges N, Ayoub F, Newman C, Quade J (2017) An integrated  
818 model for dune morphology and sand fluxes on Mars. *Earth and Planetary*  
819 *Science Letters* 457:204–212
- 820 Sauermann G, Andrade Jr J, Maia L, Costa U, Araújo A, Herrmann H  
821 (2003) Wind velocity and sand transport on a barchan dune. *Geomorphology*  
822 54:245–255
- 823 Seidel DJ, Zhang Y, Beljaars A, Golaz JC, Jacobson AR, Medeiros B (2012)  
824 Climatology of the planetary boundary layer over the continental United  
825 States and Europe. *J Geophys Res* 117:D17106
- 826 Shao Y (2008) Physics and modelling of wind erosion, vol 37. Springer Science  
827 & Business Media
- 828 Shen Y, Zhang C, Huang X, Wang X, Cen S (2019) The effect of wind speed  
829 averaging time on sand transport estimates. *Catena* 175:286–293
- 830 Sheridan PF, Vosper SB (2006) A flow regime diagram for forecasting lee  
831 waves, rotors and downslope winds. *Meteorol Appl* 13:179–195
- 832 Sherman CA (1978) A mass-consistent model for wind fields over complex  
833 terrain. *J Appl Meteorol Clim* 17:312–319
- 834 Sherman D, Farrell E (2008) Aerodynamic roughness lengths over movable  
835 beds: Comparison of wind tunnel and field data. *J Geophys Res* 113:1–10
- 836 Sherman DJ, Li B (2012) Predicting aeolian sand transport rates: A reevalu-  
837 ation of models. *Aeolian Res* 3:371–378
- 838 Smith AB, Jackson DWT, Cooper JAG (2017) Three-dimensional airflow and  
839 sediment transport patterns over barchan dunes. *Geomorphology* 278:28–42

- 840 Song Q, Gao X, Lei J, Li S (2019) Spatial distribution of sand dunes and their  
841 relationship with fluvial systems on the southern margin of the Taklimakan  
842 Desert, China. *Geomatics, Natural Hazards and Risk* 10:2408–2428
- 843 Spalding DB (1961) A single formula for the law of the wall. *Journal of Applied  
844 Mechanics* 28:455–458
- 845 Stull R (2006) 9 - the atmospheric boundary layer. In: Wallace JM, Hobbs PV  
846 (eds) *Atmospheric Science* (Second Edition), second edition edn, Academic  
847 Press, San Diego, pp 375–417
- 848 Stull RB (1988) An introduction to boundary layer meteorology, vol 13.  
849 Springer Science & Business Media
- 850 Sullivan PP, McWilliams JC (2010) Dynamics of winds and currents coupled  
851 to surface waves. *Annu Rev Fluid Mech* 42:19–42
- 852 Sweet M, Kocurek G (1990) An empirical model of aeolian dune lee-face air-  
853 flow. *Sedimentology* 37:1023–1038
- 854 Sykes RI (1980) An asymptotic theory of incompressible turbulent boundary-  
855 layer flow over a small hump. *J Fluid Mech* 101:647–670
- 856 Taylor P, Teunissen H (1987) The Askervein hill project: overview and back-  
857 ground data. *Boundary-Layer Meteorol* 39:15–39
- 858 Taylor P, Mason P, Bradley E (1987) Boundary-layer flow over low hills.  
859 *Boundary-Layer Meteorol* 39:107–132
- 860 Tsoar H, Yaalon DH (1983) Deflection of sand movement on a sinuous longi-  
861 tudinal (seif) dune: use of fluorescent dye as tracer. *Sedimentary Geology*  
862 36:25–39
- 863 Ungar JE, Haff PK (1987) Steady state saltation in air. *Sedimentology* 34:289–  
864 299
- 865 Unsworth C, Parsons D, Hardy R, Reesink A, Best J, Ashworth P, Keevil G  
866 (2018) The impact of nonequilibrium flow on the structure of turbulence  
867 over river dunes. *Water Resour Res* 54:6566–6584
- 868 Uppala SM, Källberg P, Simmons AJ, Andrae U, Bechtold VDC, Fiorino M,  
869 Gibson J, Haseler J, Hernandez A, Kelly G, et al. (2005) The ERA-40 re-  
870 analysis. *Q J R Meteorol Soc* 131:2961–3012
- 871 Valance A, Rasmussen K, Ould El Moctar A, Dupont P (2015) The physics  
872 of aeolian sand transport. *C R Phys* 16:1–13
- 873 Venditti JG, Best JL, Church M, Hardy RJ (2013) Coherent Flow Structures  
874 at Earth's Surface. John Wiley & Sons
- 875 Virtanen P, Gommers R, Oliphant TE, Haberland M, Reddy T, Cournapeau  
876 D, Burovski E, Peterson P, Weckesser W, Bright J, et al. (2020) Scipy 1.0:  
877 fundamental algorithms for scientific computing in python. *Nature methods*  
878 17:261–272
- 879 Vogelezang D, Holtslag A (1996) Evaluation and model impacts of alternative  
880 boundary-layer height formulations. *Boundary-Layer Meteorol* 81:245–269
- 881 Vosper SB (2004) Inversion effects on mountain lee waves. *Q J R Meteorol Soc*  
882 130:1723–1748
- 883 Walker I, Davidson-Arnott R, Bauer B, Hesp P, Delgado-Fernandez I, Oller-  
884 head J, Smyth T (2017) Scale-dependent perspectives on the geomorphology  
885 and evolution of beach-dune systems. *Earth-Science Review* 171:220–253

- 886 Walker IJ, Nickling WG (2002) Dynamics of secondary airflow and sediment  
887 transport over and in the lee of transverse dunes. *Prog Phys Geogr* 26:47–75
- 888 Walker IJ, Hesp PA, Davidson-Arnott RG, Ollerhead J (2006) Topographic  
889 steering of alongshore airflow over a vegetated foredune: Greenwich Dunes,  
890 Prince Edward Island, Canada. *Journal of Coastal Research* 22:1278–1291
- 891 Walker IJ, Hesp PA, Davidson-Arnott RG, Bauer BO, Namikas SL, Ollerhead  
892 J (2009) Responses of three-dimensional flow to variations in the angle of  
893 incident wind and profile form of dunes: Greenwich Dunes, Prince Edward  
894 Island, Canada. *Geomorphology* 105:127–138
- 895 Walmsley JL, Salmon J, Taylor P (1982) On the application of a model of  
896 boundary-layer flow over low hills to real terrain. *Boundary-Layer Meteorol*  
897 23:17–46
- 898 Weaver C, Wiggs G (2011) Field measurements of mean and turbulent airflow  
899 over a barchan sand dune. *Geomorphology* 128:32–41
- 900 Werner BT, Kocurek G (1999) Bedform spacing from defect dynamics. *Geol-*  
901 *ogy* 27:727–730
- 902 Wiggs G, Bullard J, Garvey B, Castro I (2002) Interactions between airflow  
903 and valley topography with implications for aeolian sediment transport.  
904 *Physical Geography* 23:366–380
- 905 Wood N (2000) Wind flow over complex terrain: a historical perspective and  
906 the prospect for large-eddy modelling. *Boundary-Layer Meteorol* 96:11–32
- 907 Zhang C, Li Q, Zhou N, Zhang J, Kang L, Shen Y, Jia W (2016) Field obser-  
908 vations of wind profiles and sand fluxes above the windward slope of a sand  
909 dune before and after the establishment of semi-buried straw checkerboard  
910 barriers. *Aeolian Res* 20:59–70
- 911 Zhang D, Yang X, Rozier O, Narteau C (2014) Mean sediment residence time in  
912 barchan dunes. *Journal of Geophysical Research: Earth Surface* 119(3):451–  
913 463
- 914 Zilker DP, Hanratty TJ (1979) Influence of the amplitude of a solid wavy wall  
915 on a turbulent flow. part 2. separated flows. *J Fluid Mech* 90:257–271
- 916 Zilker DP, Cook GW, Hanratty TJ (1977) Influence of the amplitude of a solid  
917 wavy wall on a turbulent flow. part 1. non-separated flows. *J Fluid Mech*  
918 82:29–51

919           **Local wind regime induced by giant linear dunes**  
 920           — Supplementary Material —

921   **C. Gadal\* · P. Delorme · C. Narteau · G.F.S. Wiggs · M. Baddock ·**  
 922   **J.M. Nield · P. Claudin**

923  
 924   \* Institut de Mécanique des Fluides de Toulouse, Université de Toulouse Paul  
 925   Sabatier, CNRS, Toulouse INP-ENSEEIHT, Toulouse, France.  
 926   cyril.gadal@imft.fr

927   **1. Shear velocity and calibration of the hydrodynamical roughness**

928   As the regionally predicted and locally measured velocities are available at  
 929   different heights, we can not compare them directly. We therefore convert all  
 930   velocities into shear velocities  $u_*$ , characteristic ~~of the turbulent~~ ~~the turbulent~~  
 931   logarithmic velocity profile (Spalding 1961; Stull 1988):

$$\frac{u(z)}{u_*} = \frac{1}{\kappa} \ln \left( \frac{z}{z_0} \right), \quad (15)$$

932   where  $z$  is the vertical coordinate,  $\kappa = 0.4$  the von Kármán constant and  $z_0$  the  
 933   hydrodynamic roughness. Note that, strickly speaking, this logarithmic profile  
 934   is valid for a neutrally stratified ABL only. Vertical density gradients occuring  
 935   in other conditions may thus induce large discrepancies (Monin and Obukhov 1954; Garratt 1994; Dyer 1974)  
 936   . However, as our wind measurements are in the flow region close enough to  
 937   the surface, where these effects are negligible, this logarithmic wind profile  
 938   remains a fairly good approximation in all conditions (Gunn et al. 2021). Several  
 939   measurements of hydrodynamic roughnesses are available (Raupach 1992;  
 940   Bauer et al. 1992; Brown et al. 2008; Nield et al. 2014). In the absence of  
 941   sediment transport, it is governed by the geometric features of the bed (Flack  
 942   and Schultz 2010; Pelletier and Field 2016). When aeolian saltation occurs, it  
 943   is rather controlled by the altitude of Bagnold's focal point (Durán et al. 2011;  
 944   Valance et al. 2015), which depends on the wind velocity and grain properties  
 945   (Sherman and Farrell 2008; Zhang et al. 2016; Field and Pelletier 2018).  
 946   Whether associated with geometric features or with sediment transport, its  
 947   typical order of magnitude is the millimetre scale on sandy surfaces.

948   We do not have precise velocity vertical profiles to be able to deduce an  
 949   accurate value of  $z_0$  in the various environments of the meteorological stations  
 950   (vegetated, arid, sandy). Our approach is to rather select the hydrodynamic  
 951   roughness which allows for the best possible matching between the regionally  
 952   predicted and locally measured winds, i.e. minimising the relative difference  $\delta$   
 953   between the wind vectors of both datasets:

$$\delta = \frac{\sqrt{\langle \| \mathbf{u}_{*,\text{era}} - \mathbf{u}_{*,\text{station}} \|^2 \rangle}}{\sqrt{\langle \| \mathbf{u}_{*,\text{era}} \|^2 \rangle \langle \| \mathbf{u}_{*,\text{station}} \|^2 \rangle}}, \quad (16)$$

where  $\langle \cdot \rangle$  denotes time average. This parameter is computed for values of  $z_0$  in ERA5-Land analysis ranging from  $10^{-5}$  m to  $10^{-2}$  m for the four different stations. Note that for the North Sand Sea and South Sand Sea stations, where the giant dunes feedback presumably affect the wind, we take into account the non-deflected winds only in the calculation of  $\delta$  (with a  $15^\circ$  tolerance).

As shown in Online Resource Fig. S4S3, the minimum values of  $\delta$  in the space  $(z_0^{\text{ERA5Land}}, z_0^{\text{local}})$  form a line. We thus set the roughness in the ERA5-Land analysis to the typical value  $z_0 = 10^{-3}$  m, and deduce the corresponding ones for the local stations. It leads to 2.7, 0.8, 0.1 and 0.5 mm for the Etosha West, North Sand Sea, Huab and South Sand Sea stations, respectively. Importantly, this approach somewhat impacts the calculation of the shear velocities, but not that of the wind directions. As such, most of our conclusions are independent of such a choice. However, it may affect the magnitude of the wind velocity attenuation/amplification in flow confinement situations.

## 2. Computation of the ABL characteristics

The estimation of the non-dimensional numbers associated with the ABL requires the computation of representative meteorological quantities. In arid areas, the vertical structure of the atmosphere can be approximated by a well mixed convective boundary layer of height  $H$ , topped by the stratified free atmosphere (Stull 1988; Shao 2008). In this context, one usually introduces the virtual potential temperature  $T_{\text{vp}}$ , which is a constant  $T_0$  inside the boundary layer, and increases linearly in the FA (Online Resource Fig. S12S8a):

$$T_{\text{vp}}(z) = \begin{cases} T_0 & \text{for } z \leq H, \\ T_0 \left( 1 + \frac{\Delta T_{\text{vp}}}{T_0} + \frac{N^2}{g}(z - H) \right) & \text{for } z \geq H, \end{cases} \quad (17)$$

where  $\Delta T_{\text{vp}}$  is the temperature discontinuity at the capping layer and  $N = \sqrt{g\partial_z T_{\text{vp}}/T_0}$  is the Brunt-Väisälä frequency, characteristic of the stratification. Note that, under the usual Boussinesq approximation, temperature and air density variations are simply related by  $\delta T_{\text{vp}}/T_0 \simeq -\delta\rho/\rho_0$  (see Online Resource of Andreotti et al. (2009)), so that  $N$  can equivalently be defined from the density gradient as next to Eq. 4(1).

The ERA5 dataset provides vertical profiles of the geopotential  $\phi$ , the actual temperature  $T$  and the specific humidity  $\eta$  at given pressure levels  $P$ . The vertical coordinate is then calculated as:

$$z = \frac{\phi R_t}{g R_t - \phi}, \quad (18)$$

where  $R_t = 6371229$  m is the reference Earth radius and  $g = 9.81$  m s $^{-2}$  is the gravitational acceleration. One also computes the virtual potential temperature as:

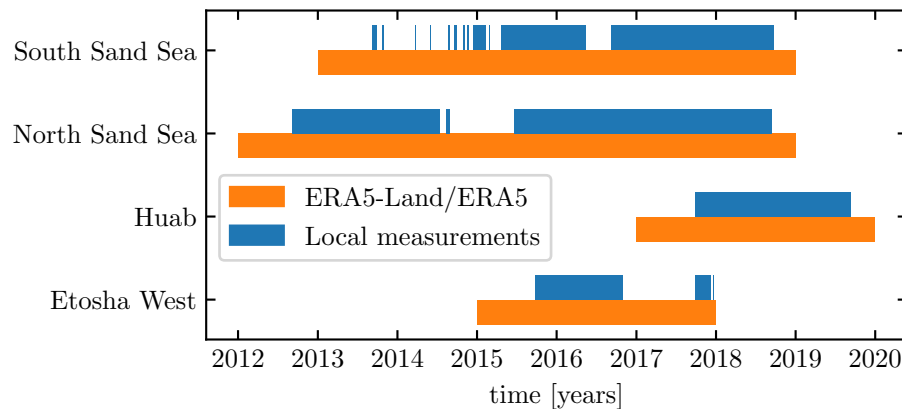
$$T_{\text{vp}} = T \left[ 1 + \left( \frac{M_d}{M_w} - 1 \right) \eta \right] \left( \frac{P_0}{P} \right)^{R/C_p}, \quad (19)$$

where  $P_0 = 10^5$  Pa is the standard pressure,  $R = 8.31$  J/K is the ideal gas constant,  $C_p \simeq 29.1$  J/K is the air molar heat capacity, and  $M_w = 0.018$  kg/Mol and  $M_d = 0.029$  kg/Mol are the molecular masses of water and dry air respectively. The specific humidity is related to the vapour pressure  $p_w$  as

$$\eta = \frac{\frac{M_w}{M_d} p_w}{p - \left(1 - \frac{M_w}{M_d}\right) p_w}. \quad (20)$$

The ERA5 dataset also provides an estimate of the ABL depth  $H$ , based on the behaviour of the Richardson vertical profile. This dimensionless number is defined as the ratio of buoyancy and flow shear terms, and can be expressed as  $\text{Ri} = N^2 / (\partial_z u)^2$ . It vanishes in the lower well-mixed layer where  $T_{vp}$  is constant, and increases in the stratified FA. Following the method and calibration of Vogelegen and Holtlag (1996); Seidel et al. (2012), the value  $\text{Ri}(z) \simeq 0.25$  has been shown to be a good empirical criterion to give  $z \simeq H$  within a precision varying from 50% for the shallower ABL (e.g. at night) to 20% for situations of stronger convection.

Examples of vertical ~~profiles of the~~ virtual potential temperature profiles deduced from ERA5 are shown in Online Resource Fig. S12S8a. For each of them, an average temperature is computed below the ABL depth ( $z < H$ ), and a linear function is fitted above, allowing us to extract the temperature jump  $\Delta T_{vp}$ . Importantly, some profiles display a vertical structure that cannot be approximated by the simple form (17) used here (Online Resource Fig. S12S8b). In practice, we removed from the analysis all of those leading to the unphysical case  $\Delta T_{vp} < 0$ . We have noticed that these ‘ill-processed’ profiles dominantly occur in winter and are evenly spread across the hours of the day. Importantly, they represent  $\simeq 12\%$  of the data only (Online Resource Fig. S12S8c,d), and we are thus confident that this data treatment does not affect our conclusions.



Gantt chart representing the valid time steps for the two data sets, for all stations.

**Fig. S1** Photographs of the meteorological stations. **a:** South Sand Sea station. **b–e:** North Sand Sea station. **d:** Huab station. **e:** Etosha West station.

Gantt chart representing the valid time steps for the two data sets, for all stations.

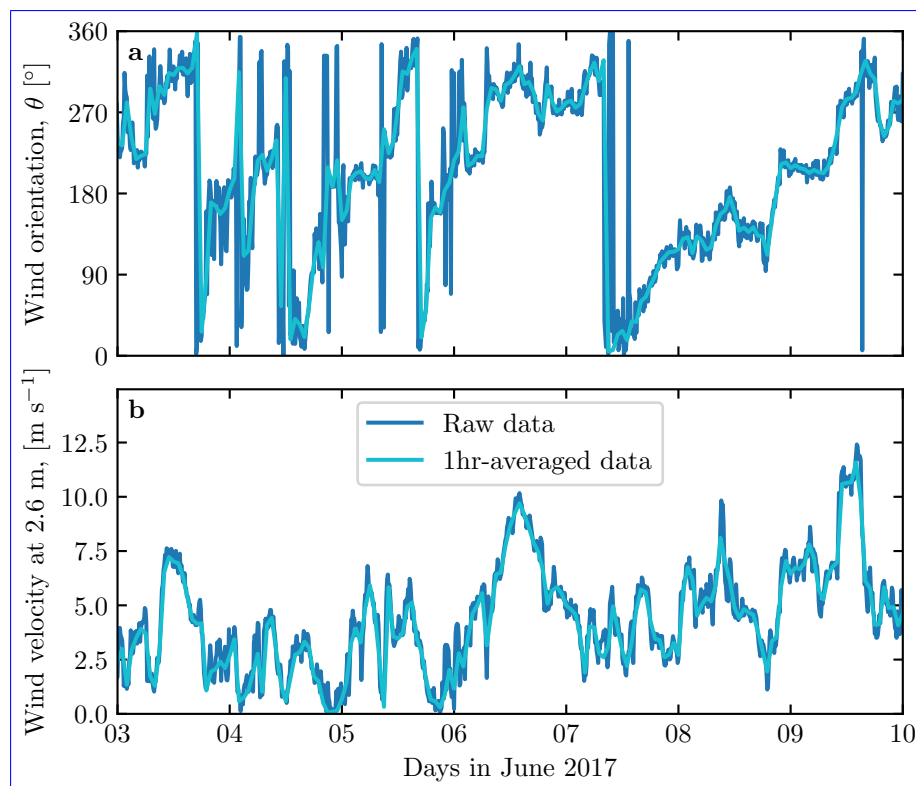


**Fig. S2** Comparison between raw local wind measurements and hourly-averaged data for South Sand Sea station. **a:** wind direction. **b:** wind velocity at height 2.6 m.

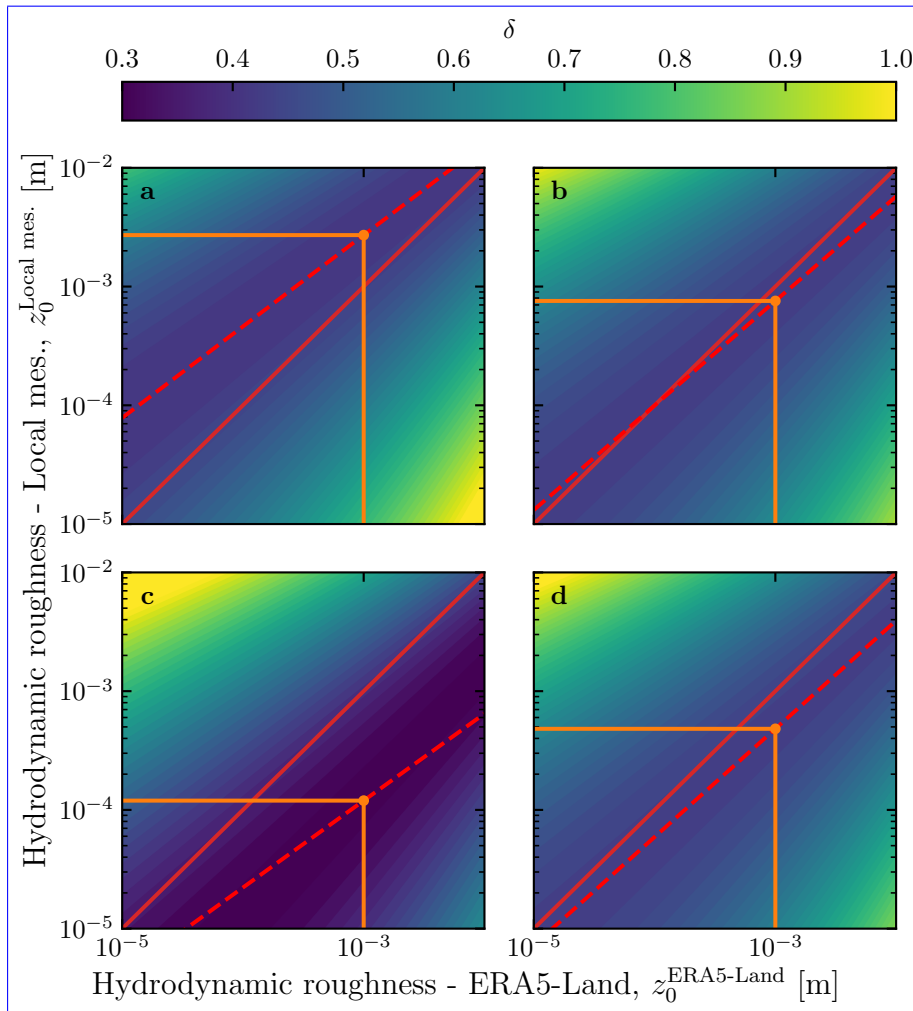


**Fig. S3** Calibration of hydrodynamic roughness. The parameter  $\delta$  (Eq. 16) quantifying the difference between local and predicted winds is shown as a function of the hydrodynamic roughnesses chosen for the ERA5-Land and for local winds, for the (a) Etosha West, (b) North Sand Sea, (c) Huab and (d) South Sand Sea stations. The red dashed and plain lines show the minima of  $\delta$  and the identity line, respectively. The orange lines and dots highlight the chosen hydrodynamic roughnesses for the local winds deduced from setting  $\underline{z_0^{\text{ERA5Land}}} = 1 \underline{z_0^{\text{ERA5Land}}} = 1$  mm.

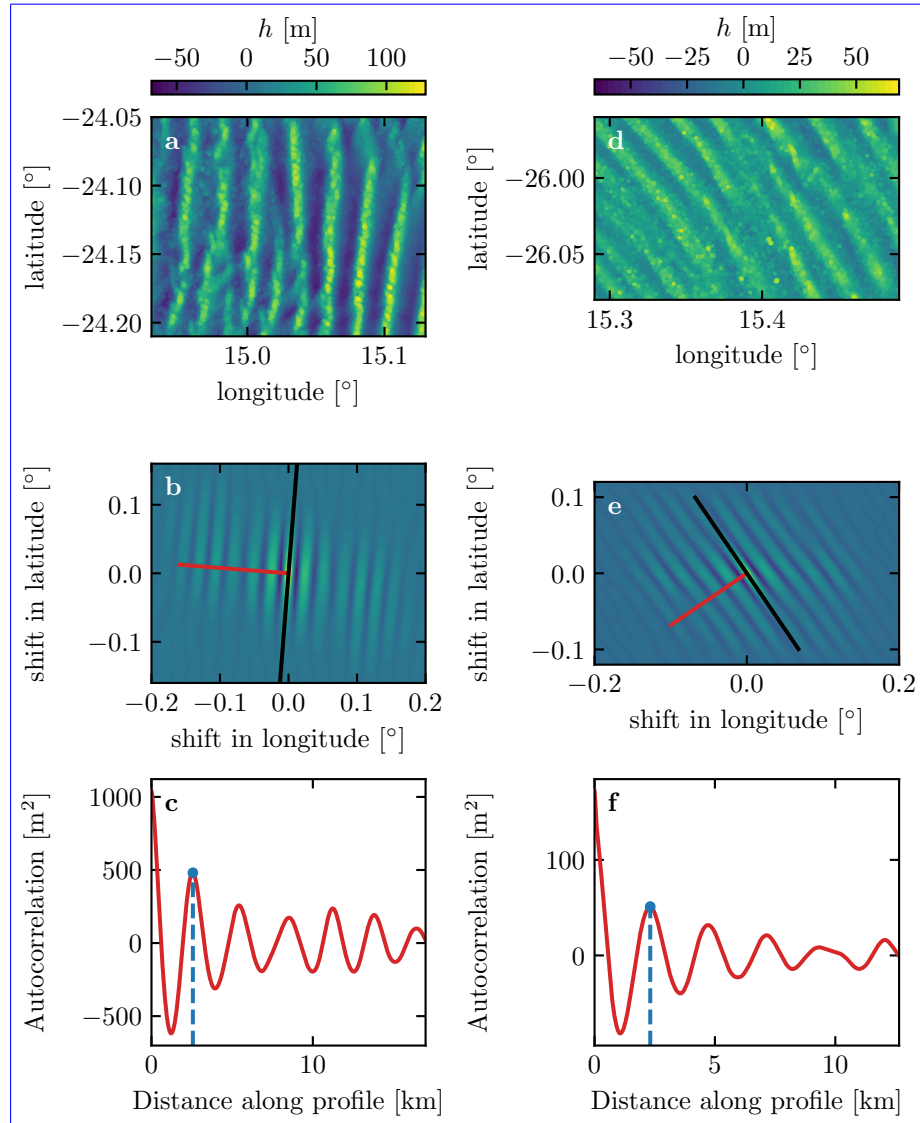


**Fig. S4** Analysis of the DEMs of the North Sand Sea (left column – panels **a**, **b**, **c**) and South Sand Sea (right column – panels **d**, **e**, **f**) stations. **a–d**: Bed elevation detrended by a fitted second order polynomial base-line. **b–e**: Autocorrelation matrix shown in **color scale**. The black line shows the detected dune orientation, and the red line represents the autocorrelation profile along which the dune wavelength is calculated, displayed in **c–f**. The blue lines and dots show the first peak of the autocorrelation profile, whose abscissa gives the characteristic wavelength of the dune pattern.

Temporal comparison between the wind data coming from the ERA5-Land climate reanalysis (orange lines) and from the local measurements (blue lines). Coloured swathes indicate day (between 1000 UTC and 2200 UTC) and night (before 1000 UTC or after 2200 UTC). **a–b**: Huab station in summer. **b–c**: Huab station in winter. **d–e**: South Sand Sea station in summer. **f–g**: South Sand Sea station in winter.

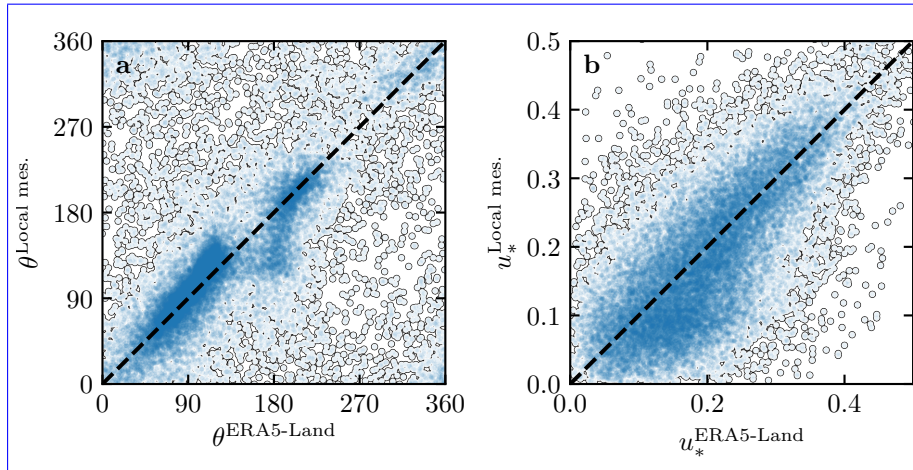


**Fig. S5** Statistical comparison of the wind orientation (a) and velocity (b) between the ERA5-Land dataset and the local measurements for the Huab and Etosha West stations. Data point clustering around identity lines (dashed and black) provide evidence for agreement of the two sets.

Distributions of wind direction at the South Sand Sea Station for the ERA5-Land climate reanalysis (orange) and the local measurements (blue)—equivalent of Fig. 3. In each subplot, both distributions are plotted from the same time steps, selected with constraints on the wind direction (columns) and/or wind velocity (rows) in the ERA5-Land dataset. The gray vertical dashed lines indicate the dune orientation. The numbers at the top centre give the percentage of time steps selected in each sub-range, as well as the percentage of them corresponding to the day (between 1000 UTC and 2200 UTC). The purple frame highlights the regime (small wind velocities, nocturnal summer wind) during which the wind data from both datasets differ.

Distributions of wind direction at the Huab and Etosha West stations for the ERA5-Land climate reanalysis (orange) and the local measurements (blue). In each subplot, both distributions are plotted from the same time steps, selected with constraints on the wind velocity (rows) in the ERA5-Land dataset. The numbers at the top centre give the percentage of time steps selected in each sub-range, as well as the percentage of them corresponding to the day (between 1000 UTC and 2200 UTC). Compared to the North and South Namib stations (Fig. 3 and Fig. S8), histograms match for high and low velocities.

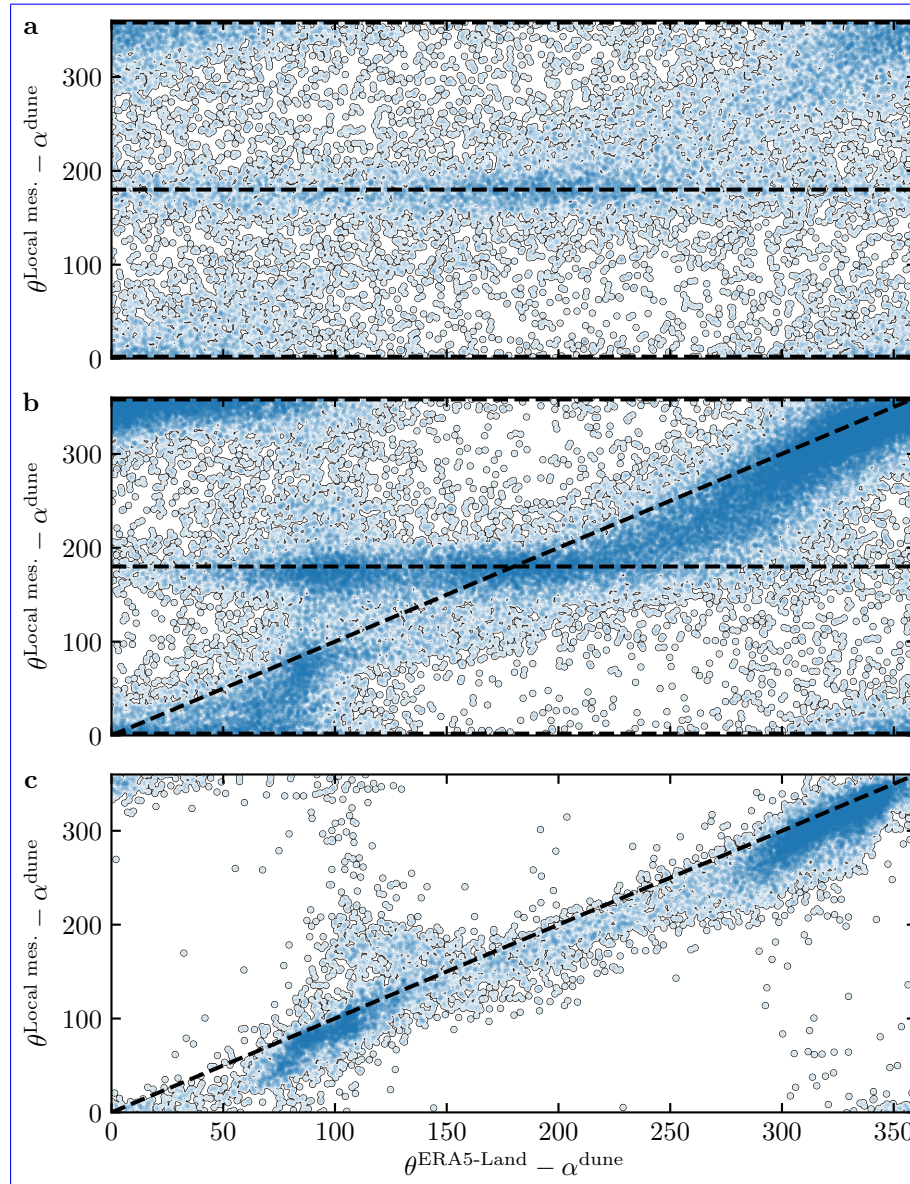


**Fig. S6** Statistical comparison of the wind orientation between the ERA5-Land dataset and the local measurements for the South Sand Sea and North Sand Sea stations, for different velocity ranges. a:  $u_{*,\text{ERA}} < 0.1 \text{ m s}^{-1}$   $u^{\text{ERA5-Land}} < 0.1 \text{ m s}^{-1}$ . b:  $0.1 < u_{*,\text{ERA}} \leq 0.25 \text{ m s}^{-1}$   $0.1 < u^{\text{ERA5-Land}} \leq 0.25 \text{ m s}^{-1}$ . c:  $u_{*,\text{ERA}} \geq 0.25 \text{ m s}^{-1}$   $u^{\text{ERA5-Land}} \geq 0.25 \text{ m s}^{-1}$ . The measured dune orientations are subtracted to the wind orientation, which allows us to plot both stations on the same graph. Black dashed lines indicate locally measured orientations aligned with the dune crests (here 0°, 180° and 360° – panels a, b), as well as the identity lines (panels b, c).

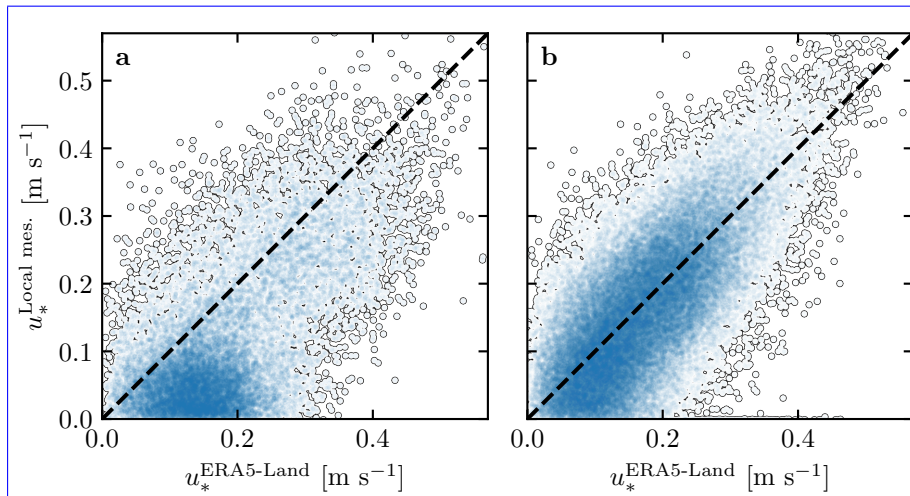


**Fig. S7** Statistical comparison of the wind velocity between the ERA5-Land dataset and the local measurements for the South Sand Sea and North Sand Sea stations. **a:** Nocturnal summer easterly wind. **b:** Diurnal southerly wind. Black dashed lines are identity lines. The angle ranges used to select diurnal and nocturnal summer winds are the same as those in [FigFigs. 3–4](#) and [Online Resourcee FigFigs. S86 of the main article](#).

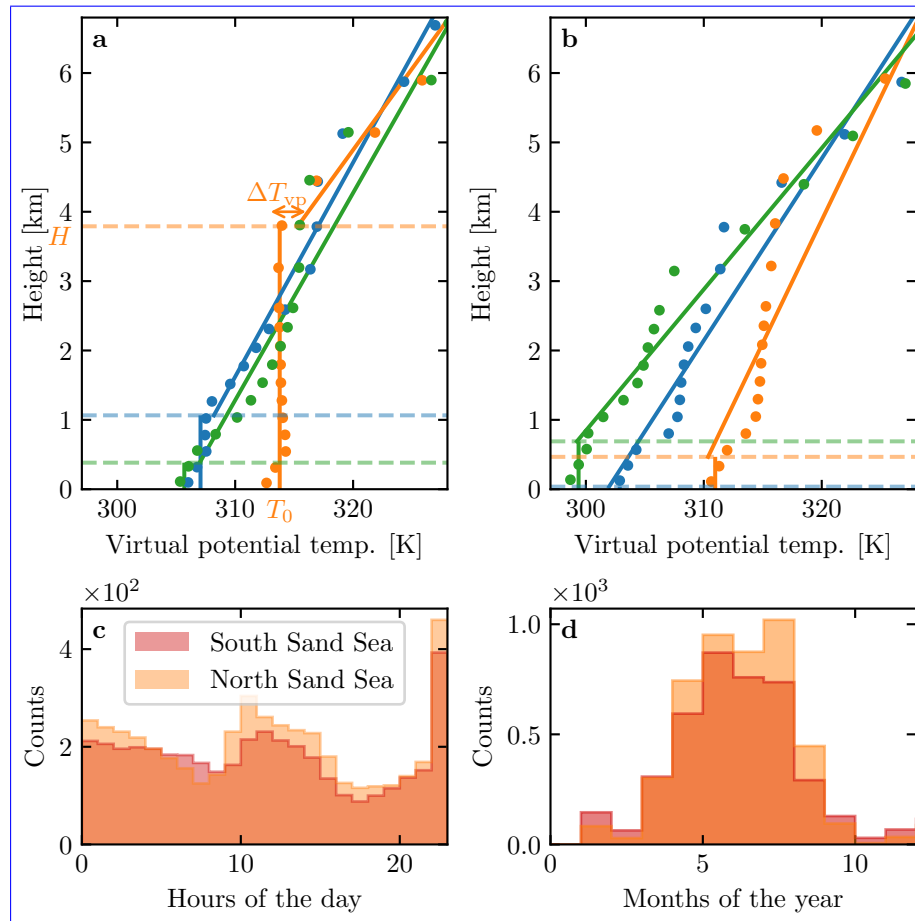


**Fig. S8** a: Vertical profiles of the virtual potential temperature at three different times (blue: 29/11/2012 - 11:00–11:00 UTC, orange: 21/03/2017 - 12:00–12:00 UTC, green: 21/03/2017 - 20:00–20:00 UTC) at the South Sand Sea station. Dots: data from the ERA5 reanalysis. Dashed lines: boundary layer height given by the ERA5 reanalysis. Plain lines: vertical (ABL) and linear (FA) fits to estimate the quantities displayed in Online Resource Fig. S13S9. b: Examples of ill-processed vertical profiles at three different times (blue: 2/12/2013 - 23:00–23:00 UTC, orange: 20/03/2017 - 00:00–00:00 UTC, green: 14/07/2017 - 14:00–14:00 UTC) at the South Sand Sea station. c: Hourly distribution Distribution of ill-processed vertical profiles dat South (orange) and North (light orange) Sand Sea station: Monthly distribution of ill-processed vertical profileshourly (c) and monthly (d) counts.

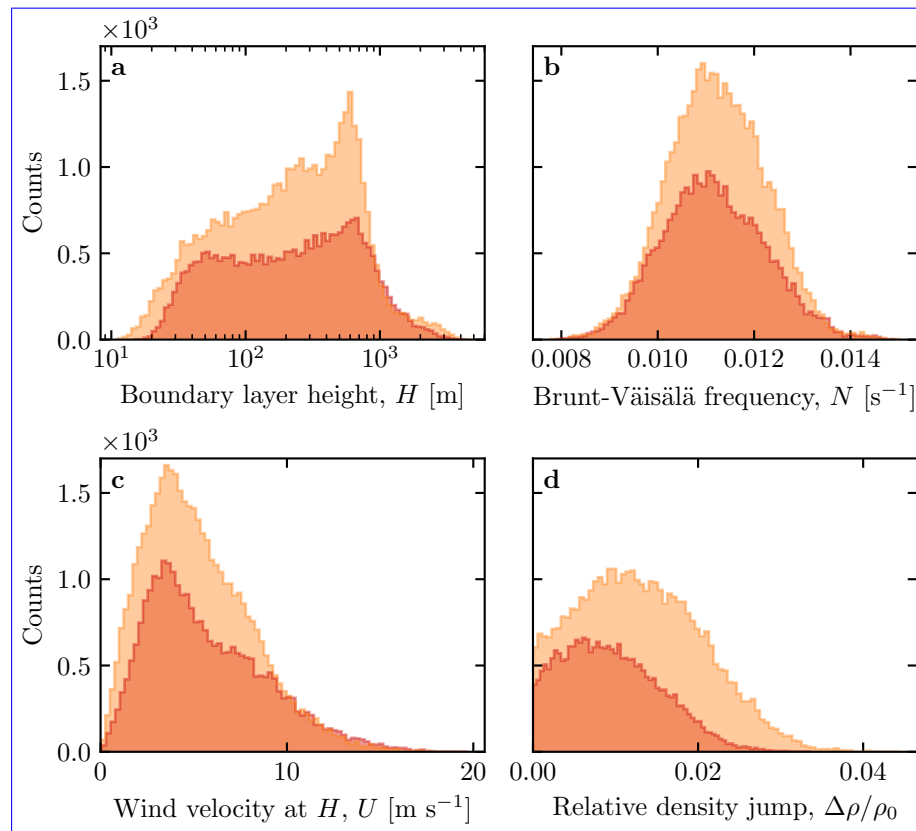


**Fig. S9** Distributions of the meteorological parameters resulting from the processing of the ERA5-Land data for the South Sand Sea (**blueorange**) and the North Sand Sea (**light orange**) stations.

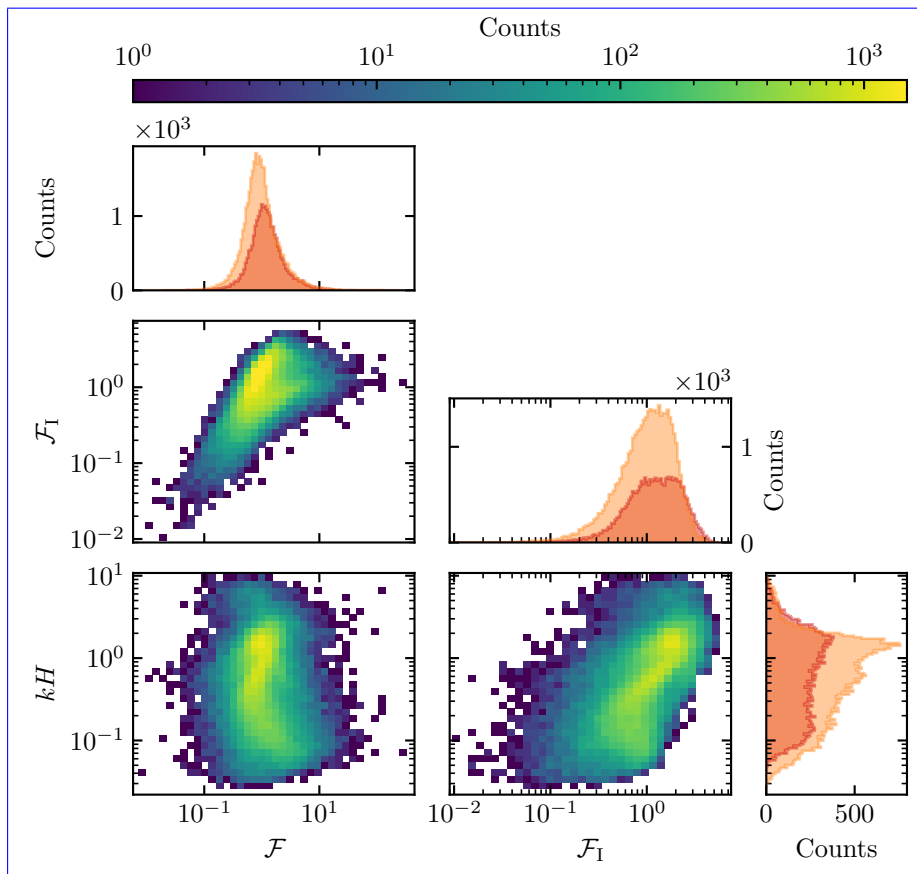


**Fig. S10** Non-dimensional parameters distributions. For the marginal distributions, the light orange corresponds to the South Sand Sea station, and the blue to the North Sand Sea station.

Regime diagrams of the wind deviation  $\delta_\theta$  and relative attenuation/amplification  $\delta_u$  in the spaces  $(\mathcal{F}_I, kH)$  and  $(\mathcal{F}_I, \mathcal{F})$ , containing the data from both the North Sand Sea and South Sand Sea stations. Green dashed lines empirically delimit the different regimes. The point density in each bin of the diagrams is shown in Online Resource Fig. S14 – 95% of the data occur in the range  $-1 < \delta u < 1$ . The similar regime diagrams in the space  $(\mathcal{F}, kH)$  are shown in Fig. 5.

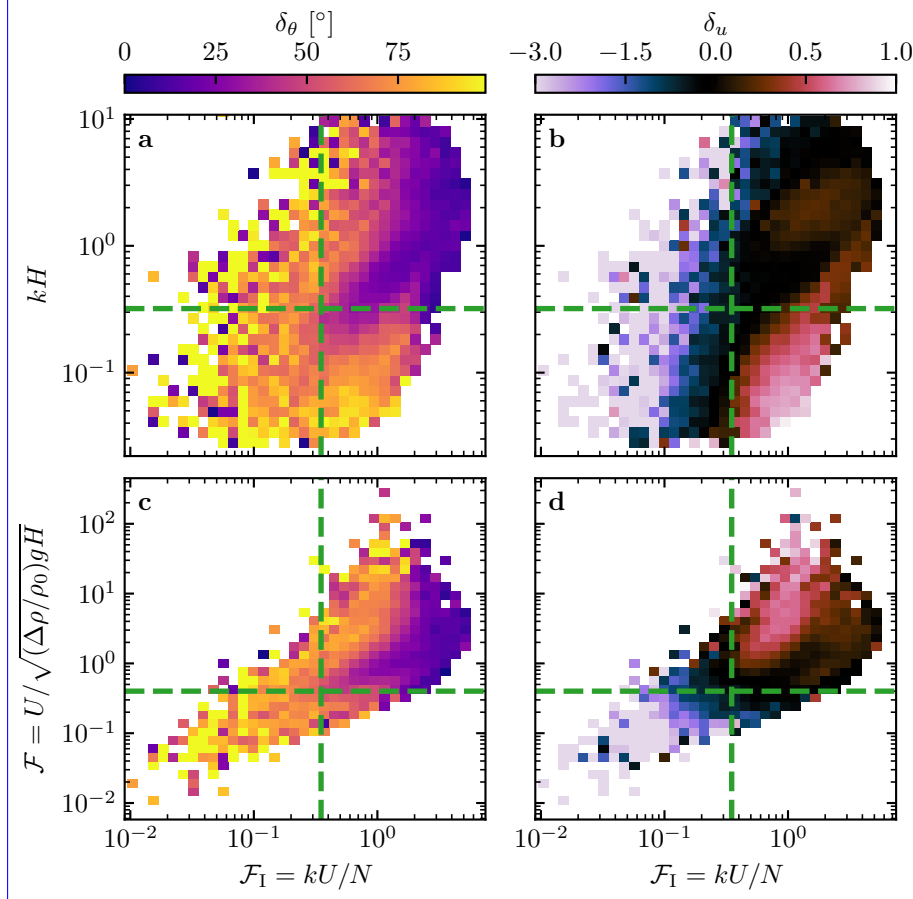


**Fig. S11** Regime diagrams of the wind deviation  $\delta_\theta$  and relative attenuation/amplification  $\delta_u$  in the spaces  $(\mathcal{F}_I, kH)$  and  $(\mathcal{F}_I, \mathcal{F})$ , containing the data from both the North Sand Sea and South Sand Sea stations. Green dashed lines empirically delimit the different regimes. The point density in each bin of the diagrams is shown in Online Resource Fig. S10 – 95% of the data occur in the range  $-1 < \delta u < 1$ . The similar regime diagrams in the space  $(\mathcal{F}, kH)$  are shown in Fig. 8.

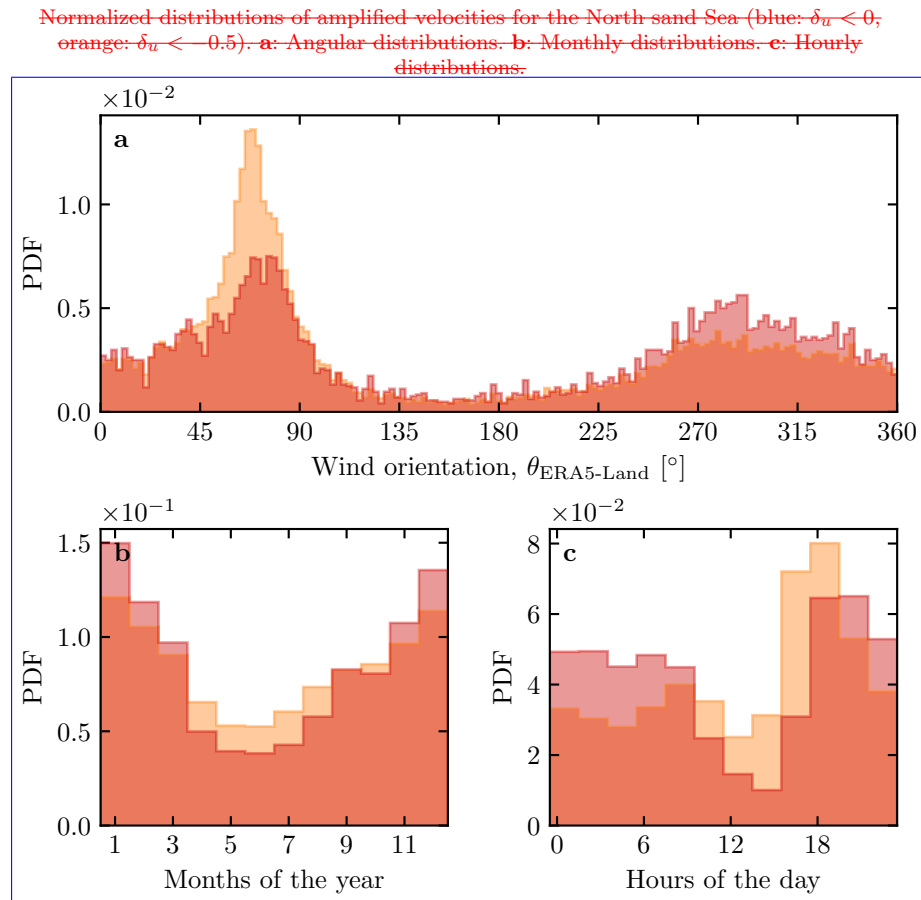


**Fig. S12** Normalized distributions of amplified velocities for the North Sea (light orange:  $\delta_u < 0$ , orange:  $\delta_u < -0.5$ ). **a:** Angular distributions. **b:** Monthly distributions. **c:** Hourly distributions.

Computation of the flow disturbance with the linear model of Andreotti et al. (2009). **a** and **b** Magnitude of the hydrodynamic coefficients  $A_0$  and  $B_0$ , calculated from the values of the non-dimensional numbers corresponding to the ERA5 Land time series presented in Figs. 4 and 5. **c** Shear velocity streamlines over sinusoidal ridges of amplitude  $k\xi_0 = 0.1$  and for increasing values of  $\sqrt{A_0^2 + B_0^2}$ . From the upper to the lower streamline, values of  $(kH, \mathcal{F}, \mathcal{F}_I, A_0, B_0, \sqrt{A_0^2 + B_0^2})$  are (1.9, 0.6, 1.5, 3.4, 1.0, 3.5), (1.5, 0.3, 0.4, 4.8, 1.4, 5.0), (0.1, 3.5, 1.0, 8.6, 0.1, 8.6), (0.5, 0.05, 0.04, 9.6, 2.5, 9.9).

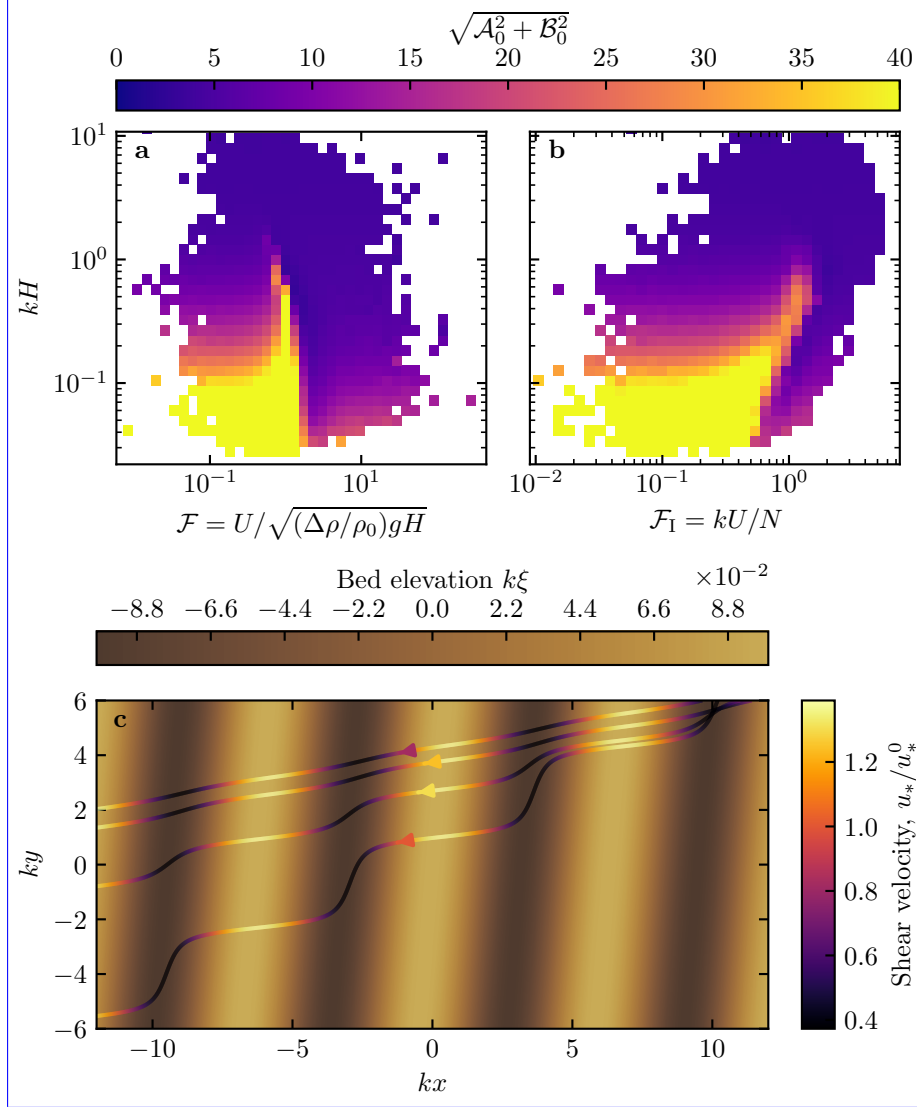


**Fig. S13** Computation of the flow disturbance with the linear model of Andreotti et al. (2009). **a–b:** Magnitude of the hydrodynamic coefficients  $A_0$  and  $B_0$ , calculated from the time series of the non-dimensional numbers corresponding to the ERA5-Land wind data and ERA5 data on vertical pressure levels. **c:** Shear velocity streamlines over sinusoidal ridges of amplitude  $k\xi_0 = 0.1$  and for increasing values of  $\sqrt{A_0^2 + B_0^2}$ . From the upper to the lower streamline, values of  $(kH, \mathcal{F}, \mathcal{F}_I, A_0, B_0, \sqrt{A_0^2 + B_0^2})$  are (1.9, 0.6, 1.5, 3.4, 1.0, 3.5), (1.5, 0.3, 0.4, 4.8, 1.4, 5.0), (0.1, 3.5, 1.0, 8.6, 0.1, 8.6), (0.5, 0.05, 0.04, 9.6, 2.5, 9.9).

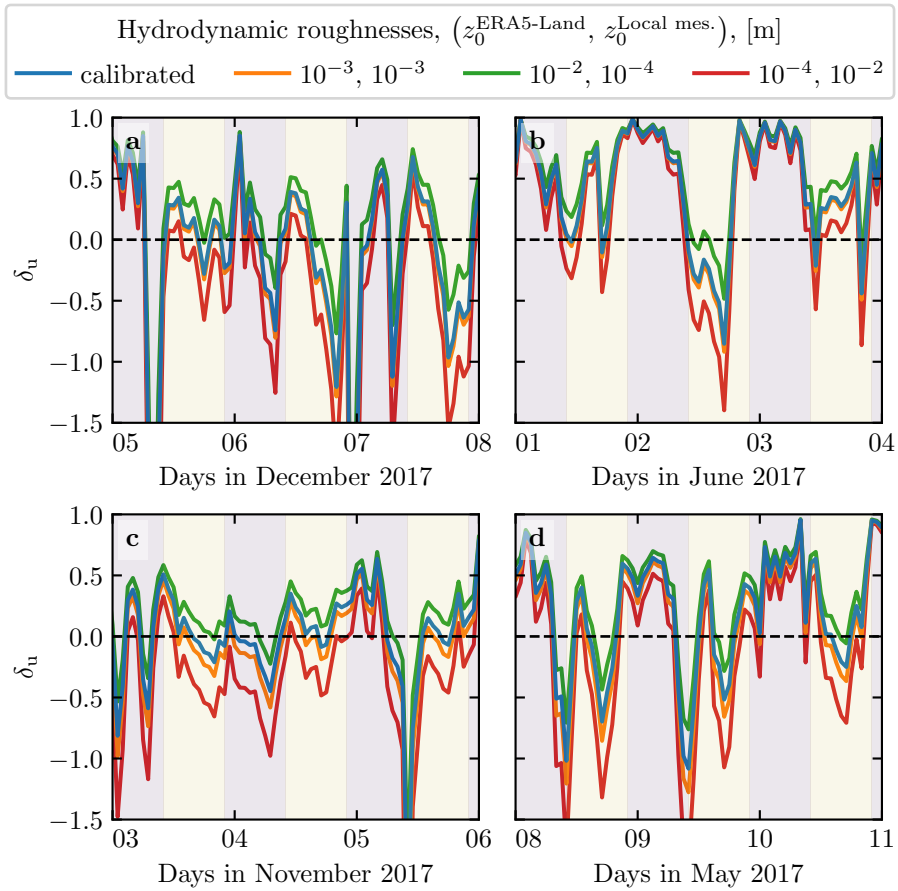


**Fig. S14** Time series of the relative velocity disturbance  $\delta_u$  corresponding to Fig. 5, for different values of the hydrodynamic roughnesses. **a:** North Sand Sea – summer. **b:** North Sand Sea – winter. **c:** South Sand Sea – summer. **d:** South Sand Sea – winter. Note that  $\delta_\theta$  is independent of the choice of  $z_0^{\text{ERA5-Land}}$  and  $z_0^{\text{Local mes.}}$ .